THEORETICAL MODELING FOR THE STEREO MISSION

MARKUS J. ASCHWANDEN
Solar & Astrophysics Lab., Lockheed Martin ATC, 3251 Hanover St., Palo Alto, CA 94304; e-mail: aschwanden@lmsal.com

L.F. BURLAGA, M.L. KAISER, C.K. NG, D.V. REAMES, M.J. REINER
NASA/Goddard Space Flight Center, Greenbelt, MD 20771

T.I. GOMBOSI, N. LUGAZ, W.IV. MANCHESTER, I.I. ROUSSEV, T.H. ZURBUCHEN
University of Michigan, 1141 Space Research Bldg., Ann Arbor, MI 48109

C.J. FARRUGIA, A. GALVIN, M.A. LEE
University of New Hampshire, EOS SSC Morse Hall, Durham, NH 03824

J.A. LINKER, Z. MIKIĆ, P. RILEY
SAIC, 10260 Campus Point Dr., San Diego, CA 92121

D. ALEXANDER, A.W. SANDMAN
Dept. Physics & Astronomy, Rice University, PO Box 1892, Houston, TX 77251

J.W. COOK, R.A. HOWARD
Naval Research Laboratory, Code 7660, 4555 Overlook Ave. SW, Washington DC, 20375

D. ODSTRČIL, V. PIZZO
NOAA/SEC, Code R/E/SE, 325 Broadway, Boulder, CO 80303

J. KÓTA
University of Arizona, Lunar and Planetary Laboratory, Tucson, AZ 85721-0092

P.C. LIEWER
Jet Propulsion Laboratory, Mail Stop 169-506, Pasadena, CA 91109

J. LUHMANN
University of Berkeley, Space Sciences Lab., 7 Gauss Way #7450, Berkeley, CA 94720

B. INHESTER, R.W. SCHWENN, S. SOLANKI, V.M. VASYLIUNAS, T. WIEGELMANN
Max-Planck Institut für Sonnensystemforschung, Max-Planck Str.2, D-37191, Katlenburg-Lindau, Germany

L. BLUSH, P. BOCHSLER
Physikalisches Institut, University of Bern, Sidlerstrasse 5, CH-3012 Bern, Switzerland

I.H. CAIRNS, P.A. ROBINSON
University of Sydney, School of Physics, Sydney, NSW 2006 Australia

V. BOTHMER
Universität Göttingen, Institut für Astrophysik, Friedrich-Hund-Platz 1, 37077 Göttingen, Germany

K. KECSKEMETY
KFKI RMKI, POB 49, H-1525, Budapest, Hungary

A. LLEBARIA
Laboratoire d'Astronomie Spatiale, C.N.R.S., BP8, 13376 12, Marseille Cedex, France

M. MAKSIMOVIC

Space Science Reviews **00:** 1–49, 2005.

CNRS & LESIA, Observatore de Paris-Meudon, F-92195 Meudon Cedex, France

M. SCHOLER
Center for Interdisciplinary Plasma Science, Max-Planck-Institute for Extraterrestrial Physics, 85740 Garching, Munich, Germany

R. WIMMER-SCHWEINGRUBER
Extraterr. Physics IEAP, University of Kiel, Leibnizstr. 11, Kiel, 24118 Germany

Received: 28 Oct 2005; Accepted in final form: ...

Abstract. We summarize the theory and modeling efforts for the STEREO mission, designed for data analysis of both the remote-sensing (SECCHI, SWAVES) and in-situ instruments (IMPACT, PLASTIC). The modeling includes the background plasma in the corona, heliosphere, and solar wind, but concentrates prominently on the dynamic phenomena associated with the initiation and propagation of coronal mass ejections (CMEs). The modeling of the CME initiation includes magnetic shearing, kink instability, filament eruption, and magnetic reconnection in the flaring lower corona. The modeling of CME propagation entails interplanetary shocks, interplanetary particle beams, solar energetic particles (SEPs), geoeffective connections, and space weather.

1. Introduction

Theoretical modeling is of particular importance for the *Solar TErrestrial RElations Observatory (STEREO)* mission because we obtain for the first time *3-dimensional (3D)* information of solar-terrestrial phenomena, which can only be exploited with realistic modeling of the 3D structure and dynamics of solar/heliospheric plasma and particles (Grigoryev 1993; Pizzo et al. 1994; Davila et al. 1996; Schmidt & Bothmer 1996; Socker et al. 1996, 2000; Rust et al. 1997; Socker 1998; Liewer et al. 1998; Howard et al. 2002; Davila & St.Cyr 2002; Mueller, Maldonado, & Driesman 2003). Table 1 yields an overview what the four instrument suites of the two STEREO spacecraft perceive: SECCHI/EUVI is imaging the solar corona, eruptive filaments, flares, and coronal mass ejections (CMEs) in the lower corona at EUV wavelengths, SECCHI/COR and HI image the CME phenomena that propagate to the outer corona in white light, and SWAVES triangulates the radio emission generated by CMEs and interplanetary shocks and particle beams. The IMPACT and PLASTIC instruments are in-situ particle detectors that measure particle distribution functions and elemental abundances at 1 AU in the solar wind or in passing CMEs, interplanetary shocks, particle beams, or in *solar energetic particle (SEP)* events. The theoretical modeling of all these processes includes both *magneto-hydrodynamic (MHD)* and kinetic theories. A great potential, but also challenge, is the unprecedented computer power that supports these theoretical and numerical modeling efforts today, never available to such a large extent in previous missions.

TABLE I
Metrics of modeled solar/heliospheric phenomena versus detecting STEREO instruments.

	SECCHI EUVI, COR/HI	SWAVES	IMPACT[1])	PLASTIC
Background Plasma:				
Solar corona (§2)	EUV,WL	...	...	...
Solar wind (§3)	...	waves	particles	particles
CME Initiation:				
Filament eruption (§4)	EUV,WL	...	...	...
Coronal mass ejection launch (§5)	EUV,WL	radio, waves	...	...
CME Propagation:				
Interplanetary shocks (§6)	WL	radio, waves	particles	particles
Interplanetary particle beams (§7)	...	radio, waves	particles	particles
Solar energetic particle events (§8)	...	...	particles	particles
Geo-connected space weather (§9)	...	...	particles	particles

[1] IMPACT will also be able to make in-situ measurements of the magnetic field at 1 AU.

We organize this review in the following order: First we describe theoretical modeling of the solar/heliospheric background plasma (solar corona in §2, solar wind in §3), then processes of CME initiation (filament eruption in §4, CME launch in §5), and then processes of interplanetary CME propagation (interplanetary shocks in §6, interplanetary particle beams and radio emission in §7, solar energetic particles in §8, geoeffective events and space weather in §9).

2. Modeling of the Solar Corona

2.1. Physical 3D-Modeling of the Global Corona

The quantitative analysis of stereoscopic EUV images requires full 3D models of the electron density $n_e(x,y,z)$ and electron temperature $T_e(x,y,z)$ of the coronal plasma, so that emission measure images $EM(x,y)$ can be self-consistently produced by integrating the *differential emission measure (DEM)* distribution, i.e., $dEM(x,y,T)/dT = \int n_e^2(x,y,z,T)dz$, along each stereoscopic line-of-sight direction z. The most detailed state-of-the-art models represent the inhomogeneous 3D solar corona with up to $\approx 10^5$ coronal loop structures, each one calculated based on a physical model (e.g., Schrijver et al. 2004). The observable input is a (synoptic) full-Sun magnetogram of the photospheric magnetic field as boundary condition, which can be extrapolated into the 3D corona by means of a potential field (source surface) model or a (non)linear force-free field model. An energy

input into the corona has to be assumed, which could be a function of the local magnetic field strength $B(x,y)$ at the footpoint and the loop length $L(x,y)$, yielding a local Poynting flux (or heating rate) of $E_H(x,y) \propto B^a(x,y)L^b(x,y)$ at position (x,y). The physical model of a coronal loop can then be specified by a hydrostatic equilibrium solution, where the heating rate is balanced by the conductive and radiative losses, e.g., the RTV solutions known for uniform heating and constant pressure (Rosner, Tucker, & Vaiana 1978), the RTVS solutions corrected for non-uniform heating and gravitation (Serio et al. 1981), or empirical scaling laws inferred from Yohkoh observations (Kano & Tsuneta 1995). The latest TRACE studies imply deviations from the equilibrium scaling laws because of the asymmetric heating functions caused by flows (Winebarger et al. 2002). The emission measures $dEM(x,y,z,T)/dT$ of the physical loops can then be filled into a datacube (x,y,z) aligned with a (stereoscopic) direction z and integrated along this line-of-sight. Full-Sun visualizations based on such physical models have been simulated for soft X-ray and EUV instruments (Fig. 1). The input parameters (such as the magnetic field model or the heating scaling law) can then be varied until the simulated images show the best match (quantified by a χ^2-value) with an observed soft X-ray or EUV image. Fitting two stereoscopic EUV images from SECCHI/EUVI simultaneously with the same physical 3D model obviously represents a very powerful method to constrain the heating function, a key observable for solving the *coronal heating problem.*

3D reconstructions of the magnetic field and electron density of the global corona have been attempted for decades (e.g., Altschuler 1979): from line-of-sight inversions of the white-light polarization (e.g., Van de Hulst 1950; Lamy et al. 1997; Llebaria et al. 1999; Quémerais & Lamy 2002), from synoptic maps combined with magnetic field extrapolations (Liewer et al. 2001), from stereoscopic image pairs in soft X-rays (Batchelor 1994), from stereoscopic or multi-frequency images in radio (Aschwanden & Bastian 1994a, 1994b; Aschwanden et al. 1995, 2004; Aschwanden 1995), from tomographic multi-image sequences in soft X-rays or EUV (Hurlburt et al. 1994; Davila 1994; Zidowitz, Inhester, & Epple 1996; Zidowitz 1997, 1999; Frazin & Kamalabadi 2005), or from DEM-tomographic multi-filter images (Frazin 2000; Frazin & Janzen 2002; Frazin, Kamalabadi, & Weber 2005). However, these reconstructions of the 3D density $n_e(x,y,z)$ of the global corona can recover only a *smoothed* density distribution, with a resolution of $\gtrsim 15^\circ$ in longitude. Such approaches can characterize the average 3D density of the background corona, but cannot be used to reconstruct elementary coronal loop structures (which require a spatial resolution of $\lesssim 1''$). However, some numerical simulation studies have zoomed into partial views of the 3D corona, rendering active regions on the level of elementary loops, based on hydrodynamic loop models (Gary 1997; Alexander, Gary, & Thompson 1998) or full-scale MHD simulations with realistic plasma heating from photospheric drivers (Gudiksen & Nordlund 2002, 2005a,b; Mok et al. 2005).

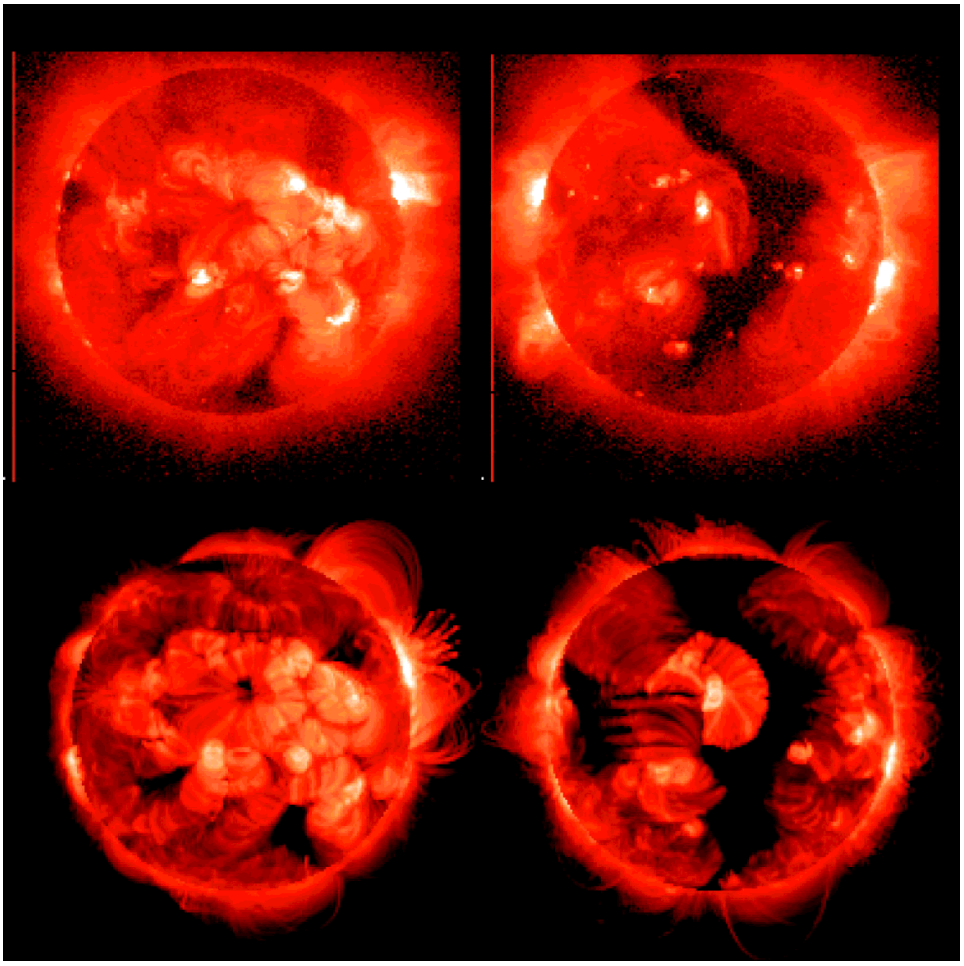

Figure 1. Full-Sun visualization of stereoscopic corona modeling: soft X-ray images from Yohkoh/SXT from two different aspect angles (top row), and simulated 3D corona images (bottom row), both shown on a logarithmic scale with a total range of 4 orders of magnitude in brightness. The theoretical 3D model is based on the observed magnetic field on the solar surface, a potential magnetic field model, a heating function, hydrostatic solutions of $\approx 50,000$ individual coronal loops, and convolution with the filter response functions (Schrijver et al. 2004).

2.2. STEREOSCOPIC 3D-RECONSTRUCTION OF CORONAL LOOPS

Although stereoscopic observations with two spacecraft provide only limited constraints for 3D modeling of the global corona, the 3D reconstruction of a single elementary loop structure should be much better constrained, if we manage to isolate a single loop by appropriate subtraction of the background corona. 3D reconstructions of elementary loop structures are of fundamental importance for studying the physical plasma properties, their (MHD) dynamics, the associated (non-potential) magnetic field and electric currents (e.g., Aschwanden 2004, §3-

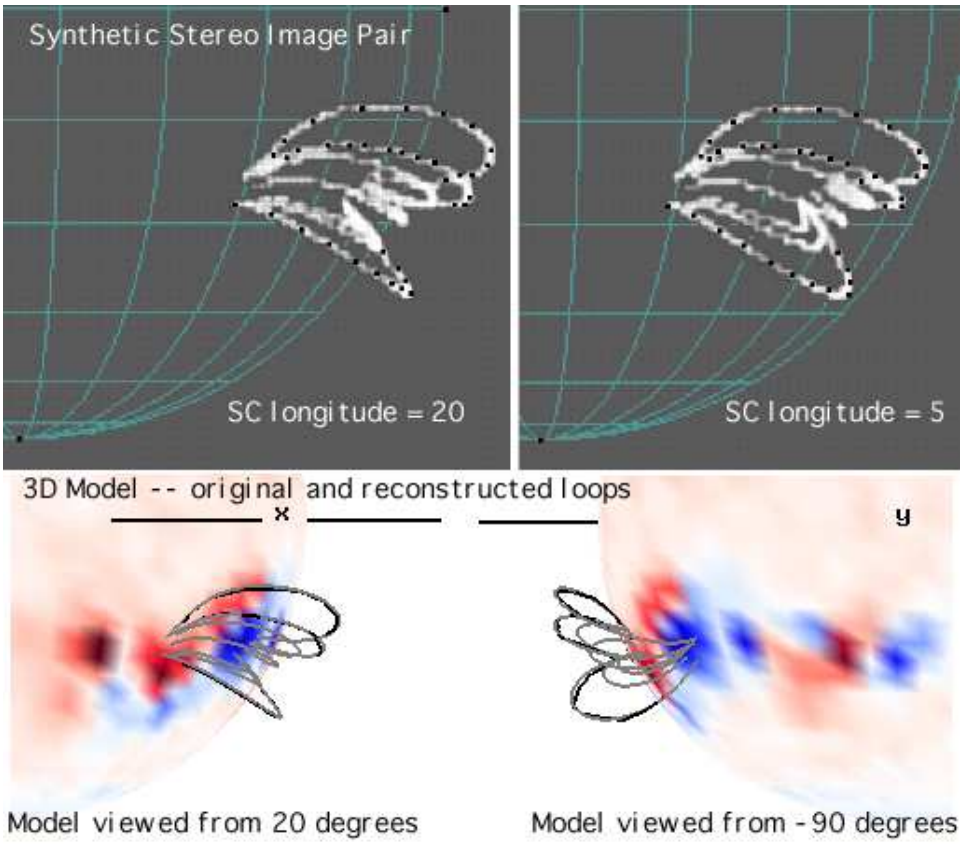

Figure 2. Stereoscopic 3D reconstruction of individual loops in EUV images using the tie-point method. Two corresponding loop structures have to be identified in a pair of images, pinpointed with tiepoints for triangulation of their 3D geometry (courtesy of Eric DeJong and Paulett Liewer).

8). The mathematical determination of the 3D geometry of a single loop has been formulated for planar loops (Loughhead, Wang, & Blows 1983) as well as for non-planar loops (Berton & Sakurai 1985). The determination of the 3D position of a point-like feature, such as the loop centroid in a particular viewing plane, is essentially a triangulation method in *epipolar planes* (Portier-Fozzani & Inhester 2001, 2002), also called *tie-point method* (Fig. 2) in some applications to solar stereoscopy (Liewer et al. 2000; Hall et al. 2004).

Such stereoscopic 3D reconstructions of single loops have been attempted in the past by using the solar rotation to mimic two different viewing angles, which of course works only for stationary loops. 3D reconstructions of single coronal structures (threads, rays, streamers) aligned with individual coronal magnetic field lines have been achieved from white-light images taken 1-3 hours apart (Koutchmy & Molodensky 1992; Vedenov et al. 2000). In order to make solar-rotation stereoscopy more general, the concept of *dynamic stereoscopy* has been developed for

the 3D reconstruction of coronal loops, which relies more on static magnetic fields, rather than on static brightness maps (Aschwanden et al. 1999, 2000). Alternative 3D reconstructions of magnetic field lines combine theoretical 3D magnetic field models with the observed 2D projection of a coronal loop from an EUV image (Gary & Alexander 1999; Wiegelmann & Neukirch 2002; Wiegelmann & Inhester 2003; Wiegelmann et al. 2005), which can be even stronger constrained by two simultaneous projections from two STEREO spacecraft. Forward-fitting techniques using some a priori constraints are expected to be superior to straightforward back-projection techniques (Gary, Davis, & Moore 1998). The efficiency of stereoscopic correlations can be considerably enhanced with automated detection of loops, e.g., with the *oriented-connectivity method* (Lee, Newman, & Gary 2005; Aschwanden 2005), with help of extrapolated magnetic field lines (Wiegelmann, Inhester, & Lagg 2005), or even by constraining the heating input with subsurface (magneto-convection) dynamics (Hurlburt, Alexander, & Rucklidge 2002). Stereoscopy of coronal loops is expected to be most suitable at small separation angles ($\lesssim 30^\circ$), which has to take place in the initial phase (during the first year) of the STEREO mission.

3. Modeling of the Solar Wind

In order to understand the propagation of CMEs and energetic particles from the corona through the heliosphere, detailed time-dependent models of the background plasma and solar wind are required. Solar wind models can be subdivided depending on their boundary conditions, either given by the magnetic field in the lower corona (§3.1), or by heliospheric conditions (§3.2). Recent space weather models involve the fully connected Sun-to-Earth system by coupling in also magnetospheric and ionospheric models, such as in the *Community Coordinated Modeling Center (CCMC)*, and these will provide the most comprehensive context for STEREO data.

3.1. Coronal Solar Wind Models

An approximate description of the global coronal magnetic field close to the Sun is given by the so-called *potential field source surface (PFSS)* model, constrained by the lower boundary condition of the photospheric magnetic field and an upper artificial boundary condition at $r \approx 1.6 - 3.25\ R_\odot$, where the magnetic field is assumed to be current-free ($\nabla \times \mathbf{B} = 0$). There exist a number or numerical codes based on such PFSS models, initially developed by Altschuler & Newkirk (1969) and Schatten, Wilcox, & Ness (1969), later refined by Hoeksema (1984) and Wang & Sheeley (1992), and recently used with input from Wilcox Solar Observatory magnetograms (at CCMC), or from *Michelson Doppler Imager (MDI)* magnetograms onboard the *Solar and Heliospheric Observatory (SoHO)* (Schrijver &

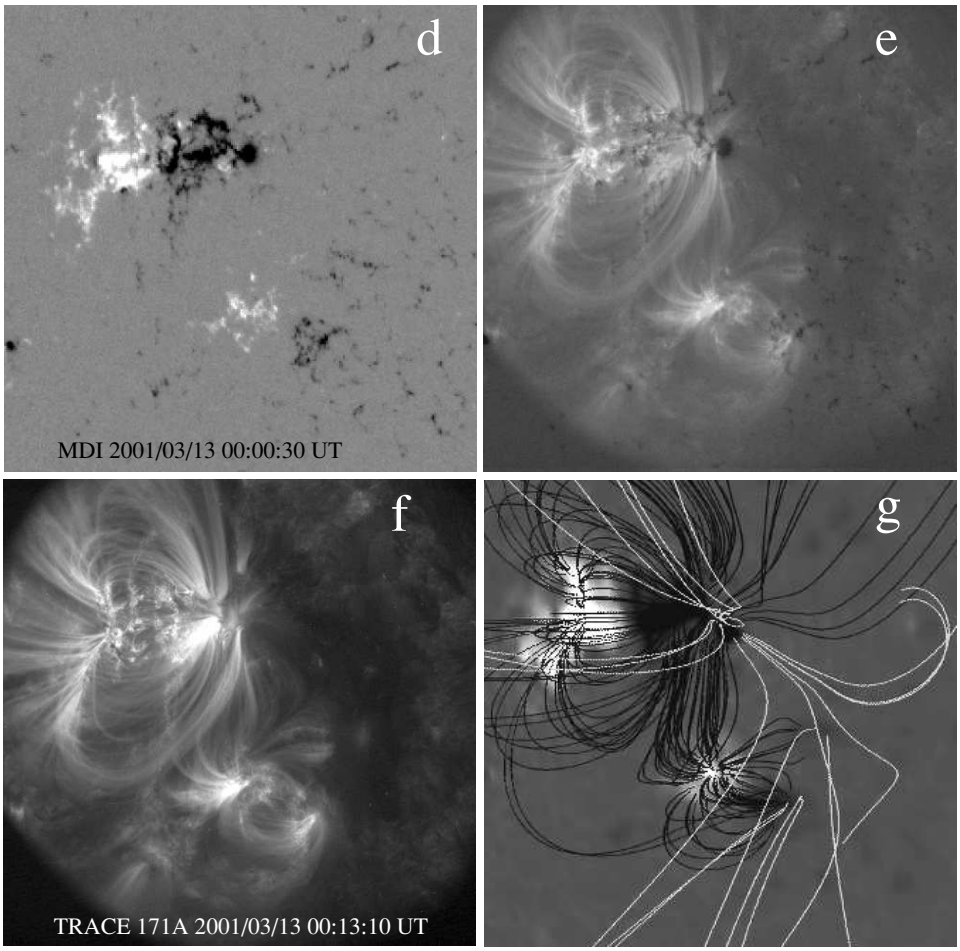

Figure 3. Panel d: MDI magnetogram; *Panel e:* MDI magnetogram overlayed with TRACE 171 Å ; *Panel f:* TRACE 171 Å image of 2001-Mar-13, 00:13 UT; *Panel g:* Potential field extrapolation using a source-surface model. Closed field lines of active regions are indicated with black color, the open field lines that connect to interplanetary space with white color (Schrijver & DeRosa 2003).

DeRosa 2003). These codes are extremely useful to map out open magnetic field regions that connect not only from coronal holes but also from some parts of active regions out into the heliosphere (Fig. 3), outlining escape paths for high-energetic particles.

The *Magnetohydrodynamics Around a Sphere (MAS)* model is developed by the *Science Applications International Corporation (SAIC)* group, which is a physics-based MHD model of the solar corona extending over a domain of 1-30 solar radii. The input of the model is (1) the radial magnetic field $B_r(\vartheta,\phi)$ as function of co-latitude ϑ and longitude ϕ from a (full-Sun) synoptic magnetogram (e.g., from *Kitt Peak National Observatory, KPNO*) that is slightly smoothed, and (2) the

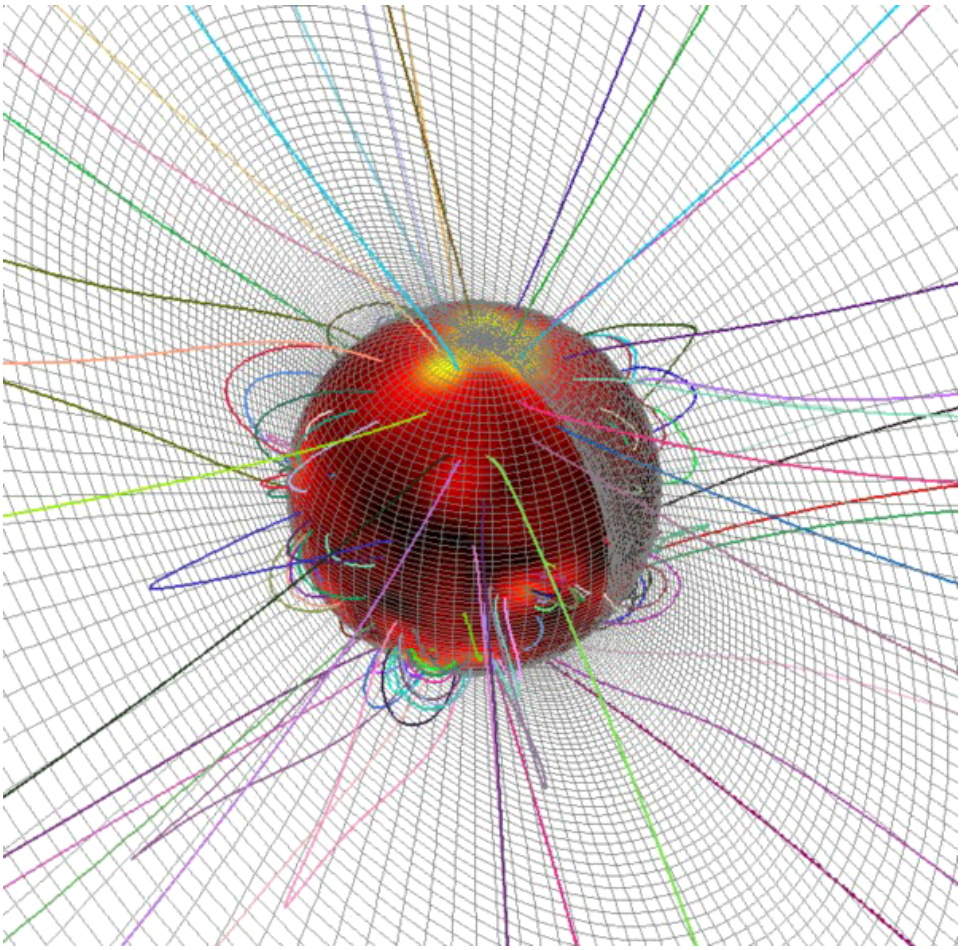

Figure 4. A 3D numerical computation of the solar corona with $101 \times 75 \times 64$ (non-uniform) meshpoints (r, ϑ, ϕ), (courtesy of SAIC group).

temperature $T_e(\vartheta, \phi)$ and density $n_e(\vartheta, \phi)$ at the coronal base. The model computes a stationary solution of the resistive MHD equations and provides as output the plasma temperature $T_e(r, \vartheta, \phi)$, pressure $p(r, \vartheta, \phi)$, density $n_e(r, \vartheta, \phi)$, solar wind velocity $v(r, \vartheta, \phi)$, and magnetic field $B(r, \vartheta, \phi)$ as function of the distance, in the range of $1 < r < 30\ R_\odot$. An example of such a 3D model is shown in Fig. 4. The MAS model has been used to simulate 3D coronal streamers (Linker, VanHoven, & Schnack 1990) and the solar corona during the *whole-Sun month* (Linker et al. 1999). Given the full 3D model of the coronal density, stereoscopic images in white-light can be integrated straightforwardly and compared with observed images from SECCHI/COR and HI.

3.2. HELIOSPHERIC SOLAR WIND MODELS

Recent numerical codes that simulate or reconstruct the solar wind in the heliosphere (e.g., Schwenn & Marsch 1991a,b; Neugebauer 2001; Balogh, Marsden, & Smith 2001) include *MAS-IP* (Riley, Linker, & Mikić 2001a; Riley et al. 2001b), *ENLIL* (developed by D. Odstrčil), *heliospheric tomography* (developed by B. Jackson & P. Hick), and the *exospheric solar wind model* (developed by H. Lamy & V. Pierrard), all part of the space weather modeling effort coordinated by CCMC. The aim of these codes is to provide components for "end-to-end models" (e.g., CISM, UMich, and CCMC) that link the coronal and solar wind physics and geometry - which is just what the STEREO combined imaging and in-situ experiments are trying to do. In the past we have had many separate coronal/imaging studies and on the other side in-situ studies. But linking them demands combined data sets and coupled corona/solar-wind models with realistic characteristics. For example, the models tell us for a particular photospheric magnetic field, where open field regions (hence solar wind sources) should be located, and which ones connect to specific points in space (e.g. STEREO and the Earth). So we can associate a particular coronal hole seen in an EUV image with a solar wind stream we detect on the spacecraft or at Earth.

The solar physics group at SAIC have developed a 3D MHD model of the solar corona and heliosphere (Riley et al. 2001a,b). They split the modeling region into two distinct parts: the solar corona (1-30 $R_{\odot}$) and the inner heliosphere (30 $R_{\odot} - 5$ AU). The combined model is driven solely by the observed line-of-sight photospheric magnetic field and can thus provide a realistic global picture of the corona and heliosphere for specific time periods of interest. Fig. 5 summarizes the global structure of the inner heliosphere for the interval coinciding with Carrington rotation CR 1913 (1996 August 22 – 1996 September 18), which occurred near solar minimum and overlapped the "Whole Sun Month" campaign. Comparisons of Ulysses and Wind observations with the simulation results for a variety of time periods (e.g., Riley, Mikić, & Linker 2003a) show that the model can reproduce the overall features of observations. In a subsequent study, the SAIC team employed this model to explore the evolution of the *heliospheric current sheet (HCS)* during the course of the solar cycle (Riley, Linker, & Mikić 2002a). They compared their results with a simple "constant-speed" approach for mapping the HCS outward into the solar wind, demonstrating that dynamic effects can sustantially deform the HCS in the inner heliosphere ($\lesssim$ 5 AU). They also noted that while the HCS may almost always be topologically equivalent to a "ballerina skirt", more complicated shapes were possible. One example was an interval approaching the maximum of solar cycle 23 (CR 1960 and 1961) when the shape would be better described as "conch shell"-like.

ENLIL is a time-dependent 3D MHD model of the heliosphere, which solves the MHD equations using a *flux-corrected-transport (FCT)* algorithm (e.g., Odstrčil et al. 2002; Odstrčil 2003). The inner radial boundary is located beyond the sonic

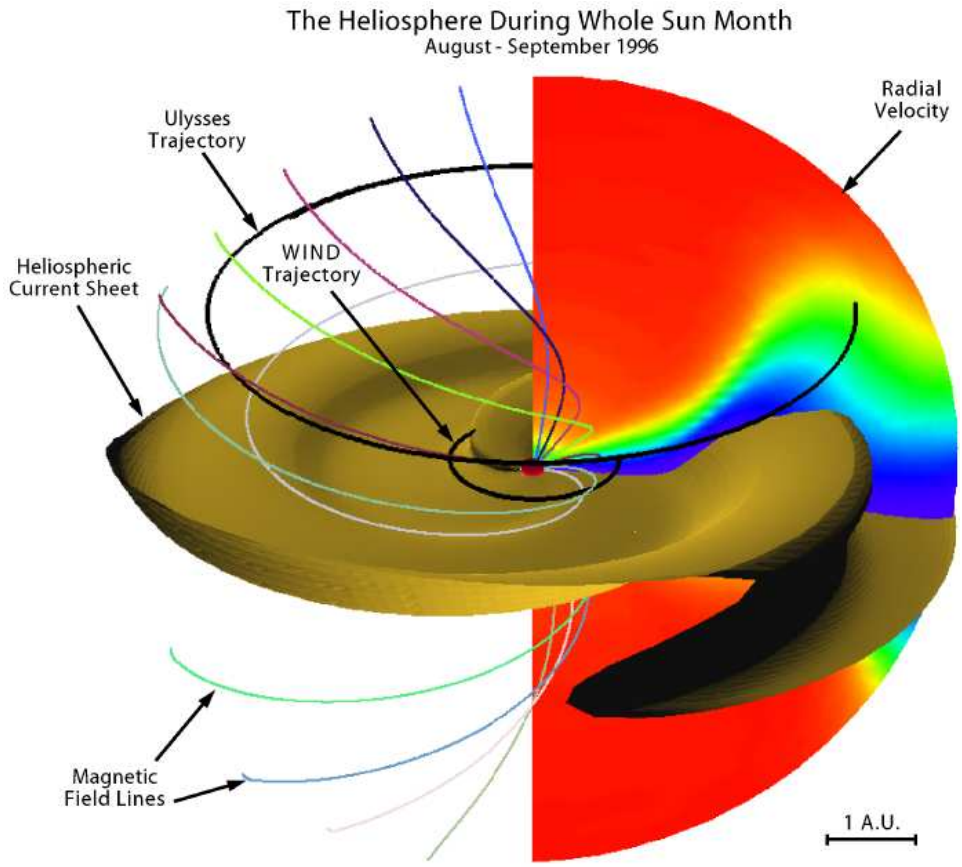

Figure 5. Model solution for Carrington rotations (CR) 1912-1913. The heliospheric current sheet (inferred from the isosurface $B_r = 0$) is displayed out to 5 AU. The central sphere marks the inner boundary at 30 $R_\odot$. A meridional slice of the radial velocity is shown at an arbitrary longitude. Blue corresponds to slowest speeds ($\approx$750 km s^{-1}). Superimposed is a selection of interplanetary magnetic field lines originating from different latitudes. Finally, the trajectories of the Wind and Ulysses spacecraft are marked (Riley et al. 2001b).

point ($\approx 21.5 - 30\ R_\odot$), provided, e.g., by the MAS or *Wang-Sheeley-Arge (WSA)* code. The outer radial boundary can be adjusted to 1-10 AU, and the latitudinal extent covers $\approx \pm 60^\circ$ north and south of the ecliptic.

In support of the STEREO mission, the CCMC is running a series of solar and heliospheric models (by coupling the MAS and ENLIL code) and is saving model input/output on a daily basis. Driven by synoptic magnetogram data obtained by ground-based solar observatories, the solar coronal potential field source surface (PFSS) model represents the approximate coronal magnetic field within 2.5 $R_\odot$. The ENLIL solar wind is driven by the WSA model (Arge & Pizzo 2000) which extends a PFSS magnetic field to 21.5 $R_\odot$ past the sonic point (where the plasma velocity starts to exceed the sound speed) using a heliospheric current sheet model

and a slow and high speed solar wind distribution depending on the location of coronal holes. ENLIL covers the radial distance between 21.5 $R_\odot$ and 1.6 AU in the inner heliosphere between $\pm 58^\circ$ degrees heliographic latitude.

In both the PFSS and ENLIL models the time stamp of each file refers to the end time of the solar rotation period covered by the magnetogram data. Typically this date lies about 2 days in the future, as magnetic fields on the solar disc can be measured fairly reliably up to 30 degrees of heliographic longitude away from the disk center (Carrington longitude of the Earth).

The *heliospheric tomography model* makes use of *interplanetary scintillation (IPS)* data to tomographically reconstruct the global structure of the solar wind, provided by earlier IPS observations from STELab in Nagoya, Japan. The model ouptut yields solar wind density and velocity throughout the inner heliosphere, and is able to make real-time heliospheric 3D reconstructions (Jackson & Hick 2002). Since January 2003, the *Solar Mass Ejection Imager Mission (SMEI)* provides data for the IPS Thomson scattering modeling of the all-sky heliospheric solar wind and CMEs (Fig. 6).

The *exospheric solar wind model* (Lamy et al. 2003) is developed for coronal holes over a radial range of $\approx 2-30\,R_\odot$, including protons and electrons, modeled with a non-monotonic total potential for the protons, and with a Lorentzian (kappa) velocity distribution function for the electrons. The exospheric kinetic model assumes that there is a critical height where there is a transition from a collision-dominated to a collisionless regime (at $\approx 1.1-5.0\,R_\odot$, called the *exobase*).

In addition to the CCMC effort, numeric codes to simulate the steady-state solar wind with helmet-type streamer belt have been developed by the MHD modeling group at the University of Michigan. An example of such a 3D MHD simulation is shown in Roussev et al. (2003a), designed to reproduce the global structure of the solar corona and wind under realistic conditions. The magnetic field in the model is split into a potential, $\mathbf{B}_0$, and a non-potential, $\mathbf{B}_1$, part: $\mathbf{B} = \mathbf{B}_0 + \mathbf{B}_1$, where $\nabla \times \mathbf{B}_0 = 0$. To obtain the bulk solar magnetic field, $\mathbf{B}_0 = -\nabla\psi$, the PFSS method by Altschuler et al. (1977) is used. In this method, the magnetic scalar potential, ψ, is evaluated as a series of spherical harmonics. The coefficients in the series are chosen to fit real magnetogram data obtained from the Wilcox Solar Observatory, and most recently from SoHO/MDI. The MHD solution in the model is evolved from a static, potential initial configuration to a steady-state, non-potential solution with a non-zero induced field, $\mathbf{B}_1$. The solar wind is powered (heated and accelerated) by the energy interchange between the solar plasma and large-scale MHD turbulence, assuming that the additional energy is stored in the "turbulent" internal degrees of freedom. Note that close to the Sun, an additional amount of energy is stored in waves and turbulent fluctuations, hence the specific heat ratio, γ, of the solar plasma is close to 1 (e.g., Steinolfson & Hundhausen 1988). The lower values of γ near the Sun are assumed to be associated with those "turbulent" internal degrees of freedom. It is assumed that $n = n_0 + n_{turb}(R)$, where the number of "turbulent"

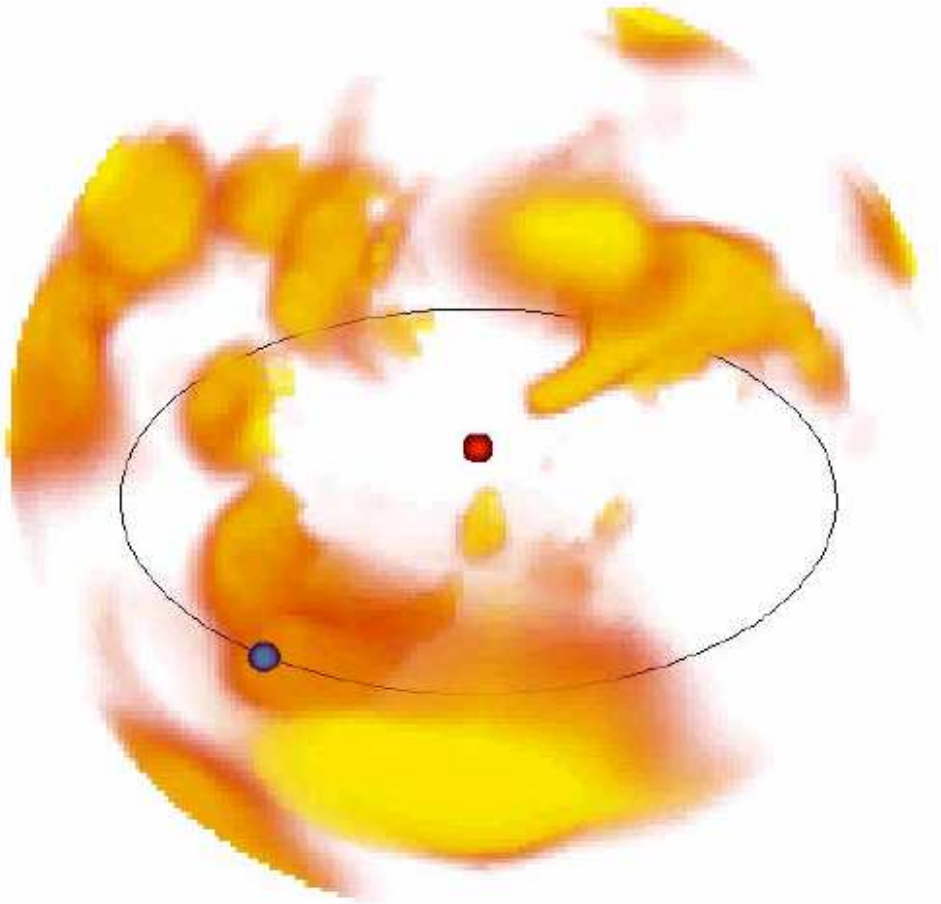

Figure 6. Time-dependent tomographic reconstruction of the solar wind using SMEI data during the 2003 May 28 CME (courtesy of Bernie Jackson).

degrees of freedom near the Sun, $n_{turb}(R_\odot)$, is ≈ 10, while at larger distances it drops to zero, i.e., $n_{turb}(\infty) \approx 0$, similar to the approach described in Zeldovich & Raizer (2002) for partially ionized plasmas. Specifically, $n_{turb}(R) = 10\,(R_\odot/R)^m$, with $m = 1$ is assumed in the original work by Roussev et al. (2003a). Thus the full energy equation is employed in the computations, with a polytropic index $\gamma(R) = [n(R)+2]/n(R)$ that is now a function of radius describing the additional energy density associated with turbulent motions. This technique is an empirical one inspired by the "hidden internal" degrees of freedom. The physical motivation is to bridge from a polytrope which is nearly isothermal to a fully fledged energy equation. The effective heating function automatically vanishes inside the helmet streamer where the bulk radial flow is suppressed ($u_R \approx 0$), a physically reasonable feature that is difficult to achieve otherwise.

The 3D models of the corona and solar wind described above will help to link IMPACT solar wind measurements to the Sun by allowing observations of specific electron populations, magnetic fields, and solar flare particle events to be mapped back to their source regions. The seven instruments of IMPACT will sample the 3D distribution of solar wind plasma electrons and the local vector magnetic field.

PLASTIC is a prime sensor on STEREO for studying coronal/solar-wind and solar-wind/heliospheric processes. It measures the distributions of density, velocity, and kinetic temperature (and its anisotropy), solar wind protons (H) and alphas (He), the elemental composition, charge state distribution, kinetic temperature, and velocity of the more abundant solar wind heavy ions (C, O, Ne, Mg, Si, Fe), as well as the distribution functions of suprathermal ions (H through Fe). The PLASTIC measurements at two different heliospheric positions will constrain better the relations between variations of the elemental composition (including the FIP effect) in the solar wind and their coronal origin, by having two spatial checkpoints at 1 AU for theoretical time-dependent 3D models of the heliospheric solar wind. The hope is to understand the acceleration of the solar wind, for instance how the slow solar wind originates near coronal streamer boundaries, or how the recurrent ion events originate near *corotating interaction regions (CIRs).*

4. Modeling of Eruptive Filaments

4.1. MHD Models of Eruptive Filaments

The trigger of a flare or CME is often the (magnetic) destabilization and subsequent eruption of a *filament* (called a *prominence* if seen over the solar limb), which is initially suspended over a highly-sheared neutral line. The destabilization of the filament can be caused either by the kink instability, during a process of increased twisting, or by some other equilibrium-loss process. It can be initiated by continued shearing of the magnetic field, by increasing currents, by converging motion of magnetic footpoints, by bouyancy with subsequent ballooning, or through new magnetic flux emergence. The physical understanding of the origin of a CME has now evolved from sketchy cartoons inspired by observations to full-scale numerical 3D MHD simulations constrained by observed magnetic fields; for recent reviews see, e.g., Forbes (2000), Klimchuk (2001), Zhang & Low (2005), and Roussev & Sokolov (2005). Let us mention a few of the most recent 3D MHD simulations that seem to be most relevant for modeling of STEREO data.

The eruption of a filament or a *magnetic flux rope* in a gravitationally confined helmet streamer cavity (in the form of cool, dense prominence material) could be initiated after draining of the prominence material. The bouyancy force causes the rise and eruption of the flux rope, pushing aside the helmet streamer field lines (Low 1996). A time-dependent 3D (ideal) MHD simulation of this CME eruption model was realized by Gibson & Low (1998), and the 3D structure viewed from

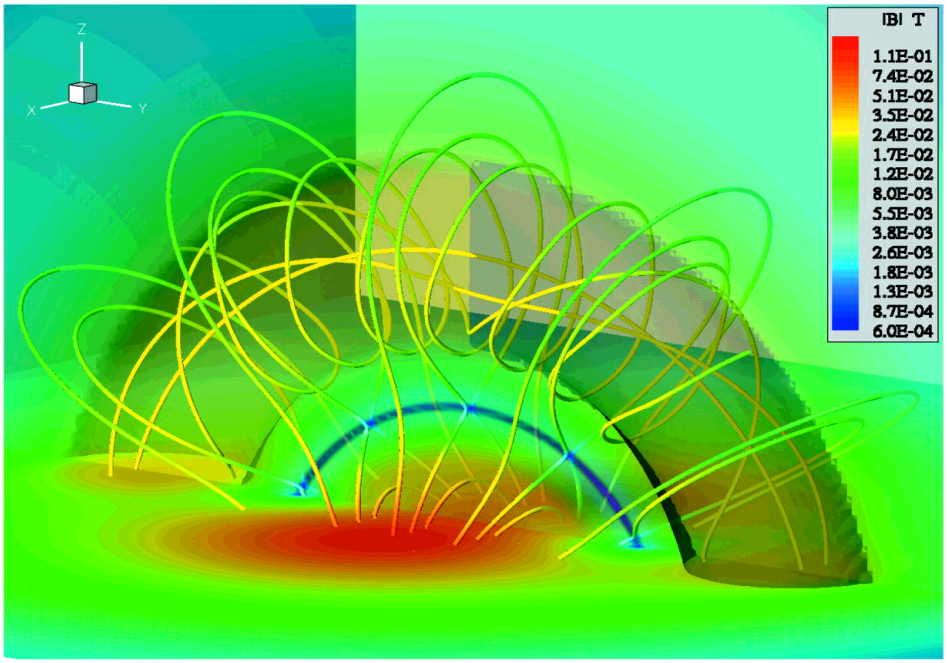

Figure 7. Initial configuration of the 3D magnetic field of a flux rope prone to loss of equilibrium and subsequent eruption. The solid lines are magnetic field lines, where the false-color code visualizes the magnetic field strength in units of Tesla. The surface shaded in gray is an isosurface at $B_z = 0$ (Roussev et al. 2003b).

different (stereoscopic) aspect angles is discussed in Gibson & Low (2000). Recent 3D MHD simulations of the *Gibson-Low model* of a buoyantly emerging magnetic flux rope are performed by Manchester et al. (2004a). The steady-state coronal field is generated from a prescribed dipole field that was partially opened up by the solar wind in the MHD model. Then a *Gibson-Low type flux rope* is inserted inside a closed magnetic loop. To initiate the filament eruption, about 20% of the balancing mass is removed from the flux rope, which produces an unbalanced pressure that brings the flux rope out of equilibrium. Future models will incorporate self-consistent arcade eruptions, based on the new insight that the magnetic field and shear velocity are not independent (Manchester 2003; Manchester et al. 2004b).

Another line of CME initiation models is based on the analytical model of Titov & Démoulin (1999), which contains a flux rope that is suspended in the corona by a balance between magnetic compression and tension forces. In the 2D models, the flux rope with current I has two possible equilibrium positions, provided that the current is not too large: The lower position is stable, while the upper position is unstable. Above a critical current there are no equilibria, and a small outward displacement leads to eruption of the flux rope. In a modified version of the Titov & Démoulin (1999) model developed by Roussev, Sokolov, and Forbes, the flux

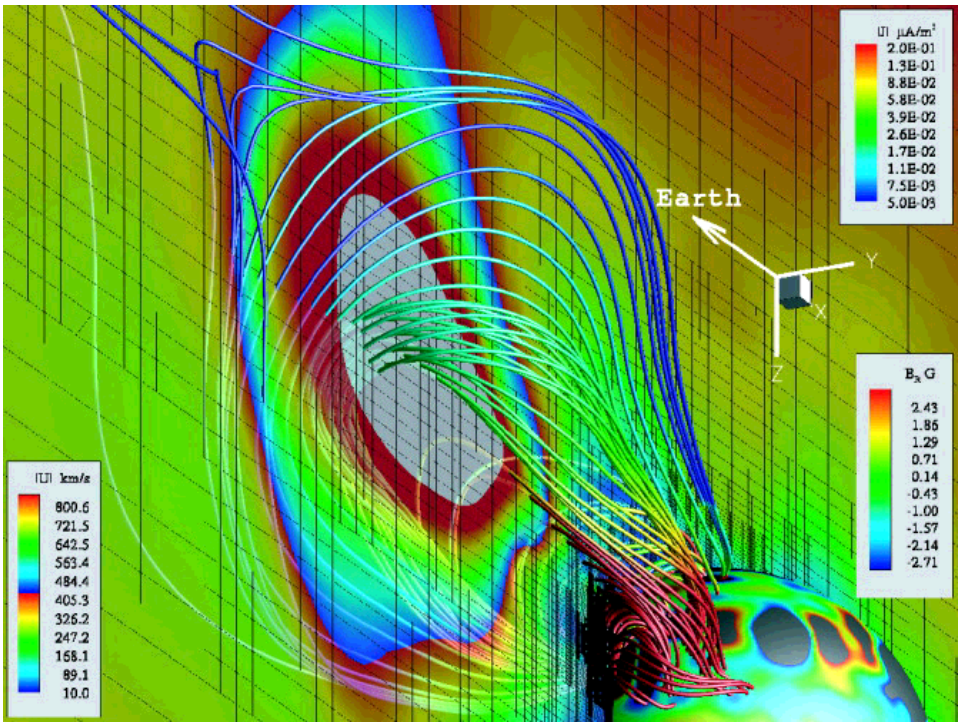

Figure 8. Three-dimensional view of the modeled CME from May 2, 1998, at 1.1 hrs after the initiation [from *Roussev et al.,* 2004]. The solid lines are magnetic field lines and the false color shows the magnitude of the current density in units of μAm^{-2} (see color legend at top right). The magnitude of flow velocity, in units of km s^{-1}, is shown on a translucent plane (see color legend to the left). Values in excess of 1,000 km s^{-1} are blanked and shown in light grey. The grid-structure on this plane is also shown as the black frame. The inner sphere corresponds to $R = R_{\odot}$. The color shows the distribution of radial magnetic field in units of Gauss (see color legend at bottom right). Regions with field strength greater than 3 G are blanked and appear in grey (Roussev et al. 2004).

rope has a poloidal force-free field produced by a (toroidal) ring current and a toroidal force-free field produced by azimuthal currents. An example of such a 3D MHD simulation of an erupting flux rope is shown in Roussev et al. (2003b), with the initial configuration illustrated in Fig. 7. A special application of this CME model is illustrated in Roussev et al. 2004 (Fig. 8). The fully 3D numerical model of a solar eruption incorporates solar magnetogram data and a loss-of-equilibrium mechanism. The study was inspired by the CME event that took place on May 2, 1998, in NOAA AR 8210 and is one of the SHINE Campaign Events. The CME model has demonstrated that a CME-driven shock wave can develop close to the Sun ($\sim 3R_{\odot}$), and is sufficiently strong to account for the prompt appearance of high-energy solar protons ($\sim$ 1 GeV) at the Earth. Using this CME model, Sokolov et al. (2004) have carried out a numerical investigation in which they quantified the diffusive acceleration and transport of solar protons at the shock wave from the

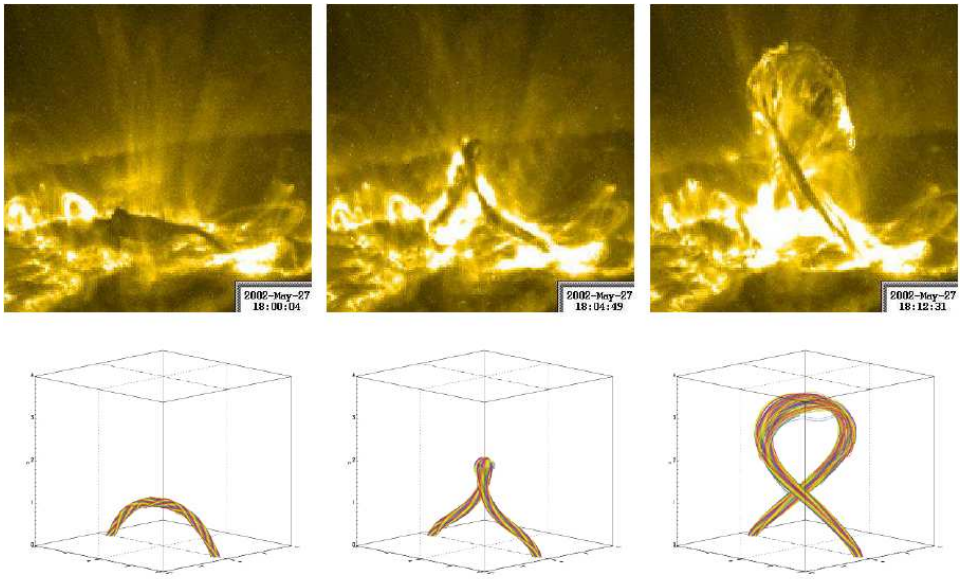

Figure 9. **Top:** TRACE 195 Å images of the confined filament eruption on 2002 May 27. The right image shows the filament after it has reached its maximum height. **Bottom:** magnetic field lines outlining the kink-unstable flux rope reproduced with 3D MHD simulations (Török & Kliem 2004).

MHD calculations. The coupled CME-SEP simulation has demonstrated that the theory of diffusive shock acceleration alone can account for the production of GeV protons during solar eruptions.

A further line of CME initiation models focuses on the kink instability of a twisted flux rope. The force-free coronal loop model by Titov & Démoulin (1999) is found to be unstable with respect to the ideal kink mode, which suggests this instability as a mechanism for the initiation of flares, once the average twist of $\Phi \gtrsim 3.5\pi$ is exceeded (Török & Kliem 2003; Török, Kliem, & Titov 2003; Kliem, Titov, & Török 2004; Rust & LaBonte 2005). A particularly fitting simulation of a kinking filament that becomes unstable is shown in Fig. 9, where a close ressemblance with EUV images from TRACE 195 Å is demonstrated (Török & Kliem 2004). The magnetic field decrease with height above the filament is critical whether a confined eruption or a full (unconfined) eruption occurs. Because this model predicts a fairly accurate evolution of the 3D geometry of the kinking filament, a time-dependent 3D reconstruction with two STEREO spacecraft using EUVI images promises very stringent tests of this theoretical model.

More complex CME initiation models involve multiple magnetic flux systems, such as in the *magnetic break-out model* (Antiochos, DeVore, & Klimchuk 1999). In this model, reconnection removes unstressed magnetic flux that overlies the highly stressed core field and this way allows the core field to erupt. The magnetic break-out model involves specific 3D nullpoints and separatrices. Such more

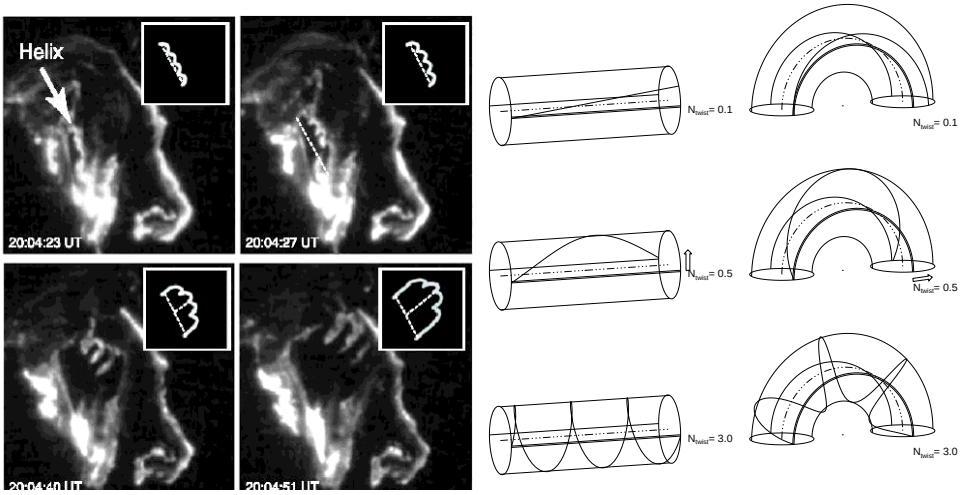

Figure 10. **Left:** TRACE 1600 Å images in C IV of the GOES-class X3 flare on 2002-Jul-15, 20:04 UT. The inserts illustrate the geometry of the helical structure, exhibiting 3 – 4 turns. Note that the helical structure expands, rises, and unwinds during the eruption (Gary & Moore 2004); **Right:** Geometrical models of helical fluxtubes with different twists (0.1, 0.5, 3.0 turns), projected onto straight and curved cylinders.

complex magnetic configurations are difficult to disentangle, but two independent views with the STEREO/EUVI imagers provide a more promising capability to test the 3D magnetic field configuration than previous single-spacecraft observations.

4.2. MODELING OF EUV AND WHITE-LIGHT EMISSION

While most theoretical models of eruptive filaments are formulated in terms of the 3D magnetic field, quantitative tests with observations require the magnetic field lines to be filled with plasma, so that emission measures and line-of-sight integrated images can be simulated and compared with observed images, e.g., in white-light for SECCHI/COR and HI, or in EUV for SECCHI/EUVI.

Previous comparisons of theoretical models with observed images of eruptive filaments showed evidence for the helical geometry of magnetic flux ropes (Rust & Kumar 1996; Chen et al. 1997, 2000; Dere et al. 1999; Wood et al. 1999; Gary & Moore 2004, Fig. 10 here), evident in EUV images in the lower corona as well as in white-light images in the outer corona. There is a strong connection between the magnetic structure of interplanetary magnetic flux ropes (or magnetic clouds) and that of the associated coronal fields at the site of erupting filaments/prominences (Bothmer & Schwenn 1998; Bothmer 2003; Cremades & Bothmer 2004). Some synthetic white-light images have been simulated for a flux rope model by Chen et al. (2000), but an unambiguous test of the 3D geometry requires at least two views with different aspect angles, as SECCHI/COR and HI will provide.

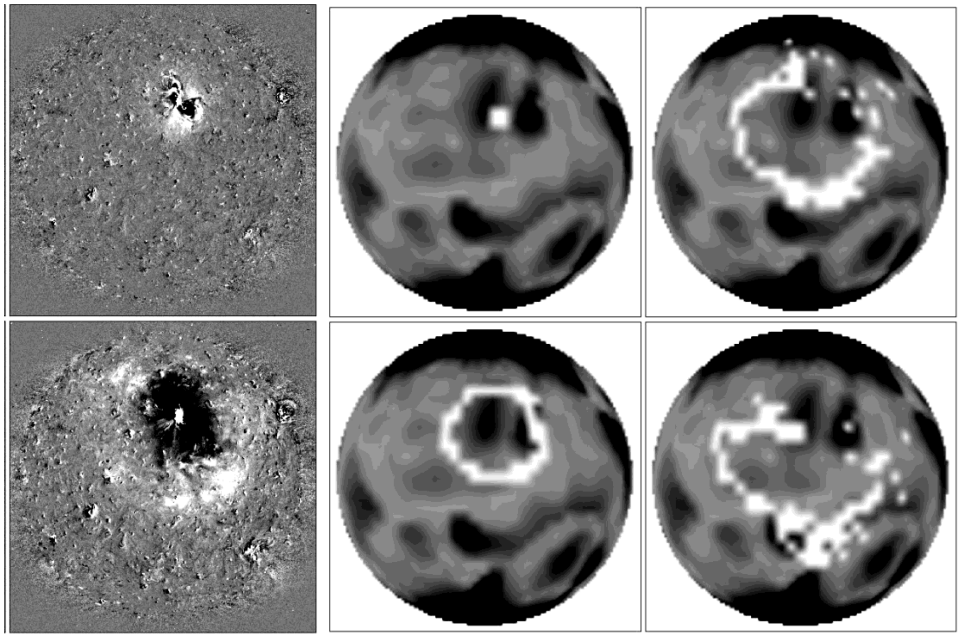

Figure 11. **Left:** Two running-difference SoHO/EIT 195 Å images of an EIT wave observed 16 min and 30 min after launch of the CME on 1997-May-12, 04:34 UT. **Right:** Simulation of an EIT wave by a ray-tracing method of fast-mode MHD waves. The color range indicates wave speeds $v > 500$ km s^{-1} (black) and lower speeds (white). The four simulated images correspond to 2 min, 15 min (middle column), and 30 min, 45 min (right column) after launch of the CME (Wang 2000).

The eruption of a filament or launch of a CME can also be tracked on the ground of the solar corona: (1) where a dimming occurs in EUV (Hudson et al. 1998) due to a temporary deficit of evacuated coronal plasma, (2) by detecting the formation of post-eruption arcades in EUV and white-light (Tripathi et al. 2004), or (3) in the form of EIT waves (Thompson et al. 1999), which concentrically propagate over the entire solar surface, caused by the *"pressure implosion"* at the epicenter of the erupted filament. The propagation of EIT waves has been theoretically simulated in terms of fast-mode MHD waves (Wang 2000; Chen et al. 2002; Wu et al. 2001), which helped to reconcile the observed speed of propagating EIT waves with the theoretically expected speeds of (fast-mode MHD) magnetoacoustic waves (Fig. 11). STEREO/EUVI images enable us to determine the average local density $n_e(\mathbf{x})$ of the coronal plasma, while photospheric magnetograms provide input for extrapolation of the coronal magnetic field $B(\mathbf{x})$, and this way the local Alfvén speed $v_A(\mathbf{x})$ and sound speed $c_S(\mathbf{x})$ can approximately be computed for every location $\mathbf{x}$ in the global corona. This allows us then to predict the (fast-mode MHD) magnetoacoustic wave speed, which in turn can be compared with the observed propagation speed of EIT waves. The SECCHI images will therefore provide powerful constraints for the 3D propagation of global waves in the corona.

The data search, the objectivity of morphological characterization, and the modeling efficiency can considerably be enhanced by automated detection algorithms, as it has already been faciliated by automated filament detection (Ipson et al. 2005; Zharkova & Schetinin 2005), by automated detection of EIT waves and dimming (Podladchikova & Berghmans 2005), by automated CME detection (Robbrecht & Berghmans 2004), and by automated detection and 3D reconstruction of EUV prominences (Foullon 2003). In summary, powerful tools for automated feature detection, theoretical 3D models of erupting filaments, and simulations of the corresponding EUV and white-light images have been developed over the last decade, but the feedback algorithms that vary the free parameters in theoretical models and control the forward-fitting to observed images (as we expect from STEREO) are still lacking.

5. Modeling of Coronal Mass Ejections

5.1. MHD Simulations of CMEs

Some key questions of the STEREO mission address the 3D structure and evolution of CMEs from the solar corona to interplanetary space, in particular the physical understanding of the forces involved in various acceleration and deceleration phases of propagating CMEs. These questions can only be answered by 3D MHD simulations of CMEs constrained by 3D observations such as those from STEREO. Powerful numerical 3D MHD codes have now become available that are capable to perform the required simulations, such as the coupled MAS/ENLIL code used by the SAIC and NOAA Team, or the BATS-R-US code used by the University of Michigan Team.

As with the ambient solar wind model described in section 3.1 and 3.2, SAIC and NOAA/SEC have coupled their models to study the eruption and evolution of CMEs through the corona and into the solar wind. The details of the algorithm used to advance the equations of the SAIC coronal models (MAS) are given elsewhere (Mikić & Linker 1994; Lionello et al. 1998, Mikić et al. 1999). Briefly, the equations are solved on a spherical (r, ϑ, φ) grid, which permits non-uniform spacing of mesh points in both r and ϑ, thus providing better resolution of narrow structures, such as current sheets. Staggered meshes are employed, which has the effect of preserving $\nabla \cdot \mathbf{B} = 0$ to within round-off errors for the duration of the simulation. The NOAA/SEC heliospheric model (ENLIL) solves the time-dependent MHD equations in a spherical geometry using either the *Flux-Corrected-Transport* or *Total-Variation-Diminishing* schemes (e.g., Odstrčil 1994; Toth & Odstrčil 1996). These high-resolution schemes produce second-order accuracy away from discontinuities, while simultaneously providing the stability that ensures non-oscillatory solutions.

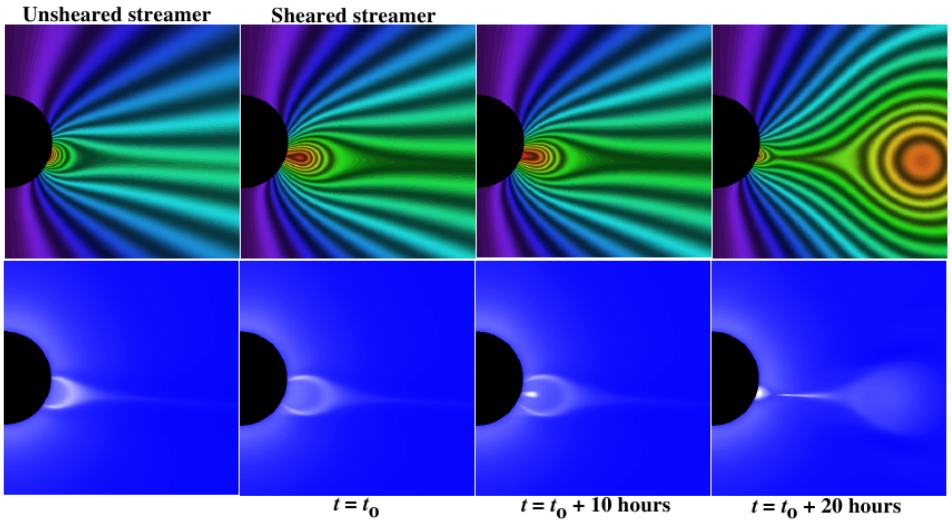

Figure 12. Evolution of a sheared helmet streamer via flux cancellation. The top panels show contours of the magnetic flux function, which in two dimensions are equivalent to the magnetic field. The bottom panels show the simulated polarized brightness. The four columns summarize: (1) the state of the unsheared corona; (2) the sheared corona; (3) the eruption of the flux rope after 10 hours; and (4) the eruption of the flux rope after 20 hours, respectively (Riley et al. 2003b).

Fig. 12 illustrates how CME initiation can be modeled self-consistently. The configuration of the solar corona prior to the emergence of the flux rope is summarized in the two left most panels. This type of equilibrium solution has been discussed in more detail by Linker et al. (1999). Contours of the magnetic flux function (fiduciaries of magnetic field lines in two dimensions) are shown by the solid lines and shaded contours (Fig. 12, top). The system consists of a single streamer belt displaced by $\approx 10^{\circ}$ below the heliographic equator. The first column shows the state of the corona after the system has reached equilibrium. The second column shows how this configuration is modified by energization of the magnetic field via photospheric shear (Linker & Mikić 1995). At this point, the system is still in equilibrium. The polarized brightness (pB) is shown in the Fig. 12 bottom panels, constructed by integrating the product of the number density with the scattering function (Billings 1966) along the line-of-sight (see Section 5.3). The resulting image bears a strong generic resemblance to SoHO/LASCO white-light images taken near solar minimum. The remaining panels of Fig. 12 summarize the lauch of a flux rope following the cancellation of flux. As can be seen, the origins of the flux rope lie in the closed magnetic field lines embedded within the streamer belt. As the flux rope erupts into the solar corona, overlying field lines, which are still connected back to the Sun at both ends, are brought together under the flux rope. As they reconnect with each other, they contribute both to the flux of the evolving flux rope to the right of the reconnection site and to the re-growth of the streamer belt to the left. Note that the flux rope has developed an elliptical shape, with its major

axis approximately horizontal. Note also that the reconnection site underneath the erupting flux rope is visible in the simulated pB image at $t = 20$ hours. This density enhancement was produced by the vertical (i.e., approximately parallel to the solar surface) flow of plasma into the reconnection region and has been observed in white light images (Webb et al. 2003). With regard to the simulated polarized brightness images, we also remark that they bear a strong resemblance to the classic three-part structure of CMEs observed in white light: the bright front, dark cavity, and dense core.

The BATS-R-US code solves a set of (ideal) MHD equations using the *Block Adaptive Tree Solar Wind Roe-type Upwind Scheme (BATS-R-US)* code (Powell et al. 1999; Groth et al. 2000), in combination with the *Artificial Wind approximate Riemann (AWR)* solver (Sokolov et al. 2002). This is a conservative finite-volume method with shock-capturing total variation diminishing schemes, explicit/implicit time stepping, a block-adaptive mesh refinement scheme, that runs on massively parallel computers. The energy equation is simplified by neglecting radiative losses, heat conduction, and background heating. Also dissipative effects due to viscosity and electric resistivity are not included, but the code has some numerical dissipation. A series of BATS-R-US runs simulate the launch of a CME by loss of equilibrium of a flux rope anchored on the solar surface (Roussev et al. 2003b), shock formation at a distance of 5 $R_\odot$ (Roussev et al. 2004), and the evolution of the CME density structure during propagation out to 100 $R_\odot$, with simulations of stereoscopic views in white-light (Figs. 13) as it will be seen by STEREO/HI-2 (Lugaz, Manchester, & Gombosi 2005).

The ENLIL code, described in the foregoing section on the solar wind (§3.2), is a heliospheric code developed by the NOAA Team (Odstrčil et al. 2002) and covers the range from 30 $R_\odot$ to 1-5 AU, using input at the lower boundary from the MAS model that extends from 1 to 30 $R_\odot$. The heliospheric code is somewhat simpler than the coronal code (which requires to solve the resistive MHD equations), because the ambient solar wind is everywhere super-critical and the ideal MHD equations can be used. This heliospheric code (Odstrčil et al. 1996; Toth 1996; Odstrčil & Pizzo 1999a,b) solves the ideal MHD equations with an explicit finite-difference scheme, uses an adiabatic constant of $\gamma = 5/3$ to describe the fully-ionized solar wind plasma, and produces accurate shock strengths. This code simulates the distortion of the interplanetary magnetic field by the 3D propagation of a CME in a structured solar wind (Odstrčil & Pizzo 1999a), the 3D propagation of a CME launched within (Odstrčil & Pizzo 1999b) and adjacent to a streamer belt (Odstrčil & Pizzo 1999c) out to 5 AU. These runs have shown that the disentangling of merged CME and CIR shocks require multi-spacecraft observations such as STEREO will provide. Simulations of the 12 May 1997 *interplanetary coronal mass ejection (ICME)* event have enabled us to predict the arrival of the shock and ejecta at Earth (Odstrčil, Riley, & Zhao 2004a). Stereoscopic white-light images

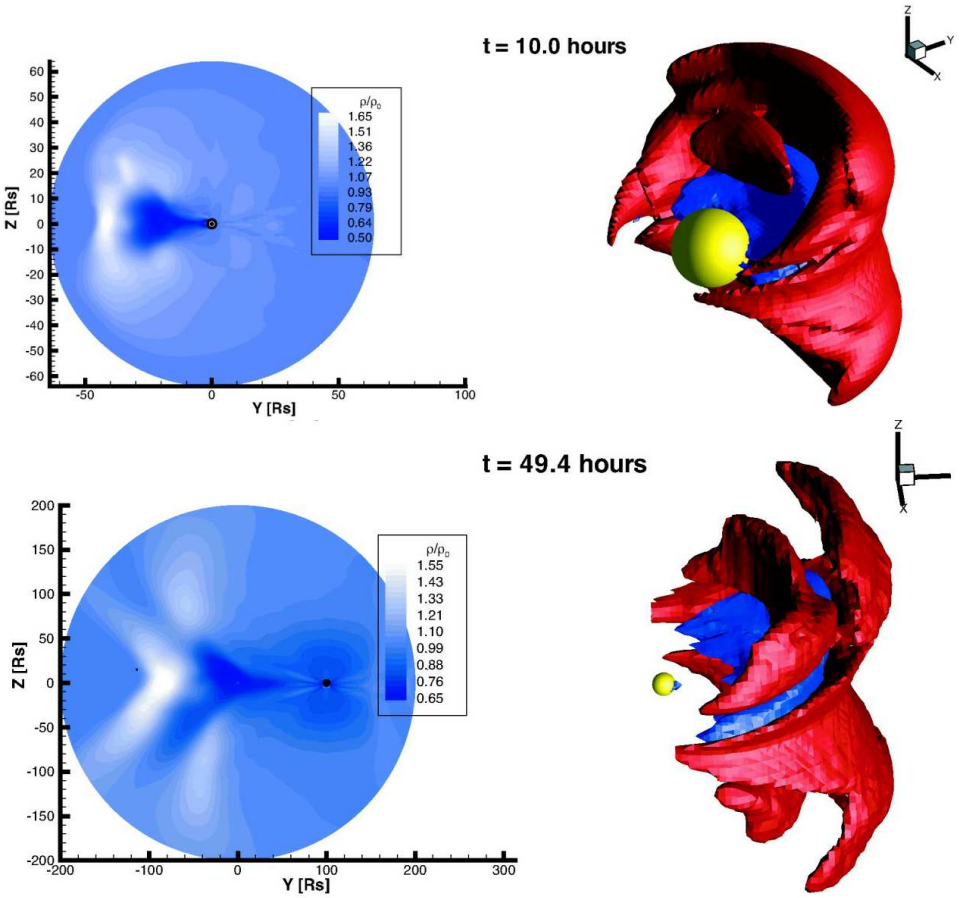

Figure 13. **Top left:** Line-of-sight image of a CME simulated with the BATS-R-US code, 10 hours after its launch, as seen from a coronagraph looking at the limb CME with a field of view of 64 $R_\odot$ centered at the Sun. The black disk, corresponding to 2 $R_\odot$, shows the occulting disk of the coronagraph. **Top right:** Two isosurfaces showing the density increase by 30% (red) and a density decrease of 20% (blue) over the pre-event density structure, 10 hr after launch of the CME. The yellow sphere is positioned at the Sun and has a radius of 10 $R_\odot$. **Bottom left:** Line-of-sight image of the CME, 49.6 hours after launch, with a field-of-view of 200 $R_\odot$. **Bottom right:** Similar representation as top right, at 49.6 hours after launch (Lugaz, Manchester, & Gombosi 2005).

simulated from these 3D MHD outputs are expected to allow for discrimination between different event scenarios (Odstrčil, Pizzo, & Arge 2005).

The most comprehensive end-to-end approach of modeling CMEs has been started at the *Center for Integrated Space Weather Modeling (CISM)*, led by Boston University (Principal Investigator: W. J. Hughes). The goal is to simulate the full Sun-to-Earth system by coupling state-of-the-art codes (Luhmann et al. 2004), modeling the solar corona (MAS code), the solar wind (ENLIL code), the magnetosphere, and the upper atmosphere/ionosphere. The propagation of a CME in

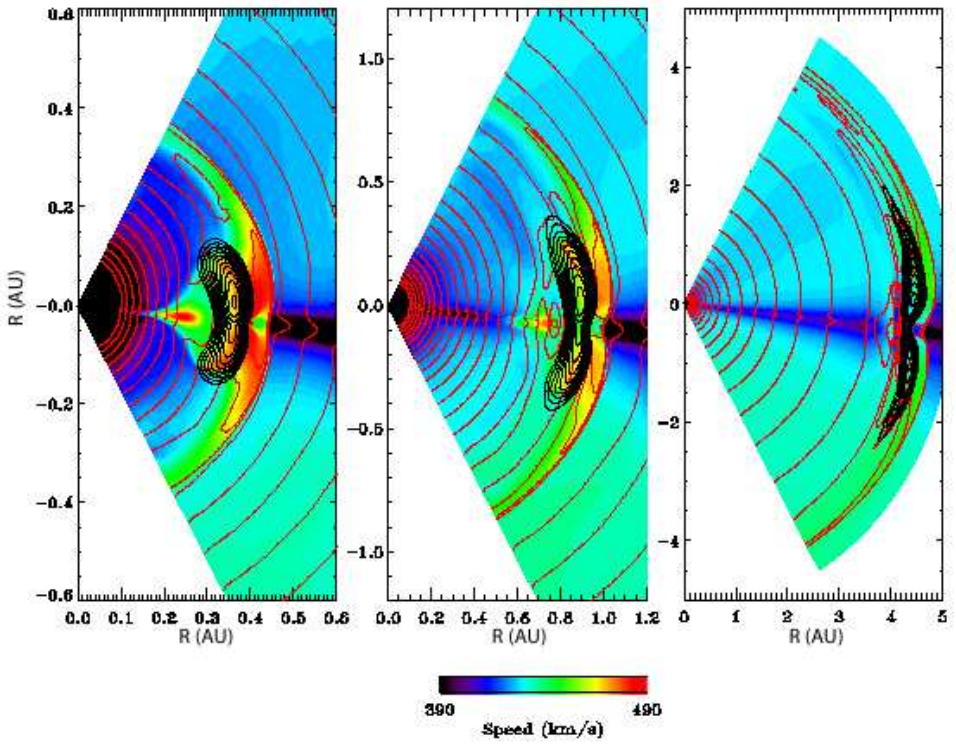

Figure 14. Evolution of a flux rope through the inner heliosphere. The panels extend $\pm 60°$ in latitude and from left to right, extend in heliospheric distance from the Sun to 0.6 AU, 1.2 AU, and 5 AU. The contours denote: radial velocity (color); density (red lines); and magnetic field (black lines). (Riley et al. 2003b).

a coupled coronal (MAS) and heliospheric (ENLIL) MHD code is decribed in Odstrčil et al. (2004b).

Fig. 14 summarizes the evolution of a flux rope and its associated disturbances between the Sun and 5 AU at 3 times. The displayed speeds have been restricted to 390-490 km s^{-1} to emphasize flows associated with the disturbance. Note how the ejecta becomes progressively more distorted with increasing heliocentric distance. By ≈ 5 AU it has been squeezed so much at low latitudes that it has evolved into two lobes, connected by a thin band of compressed field. Surprisingly, much of this distortion can be described by kinematic effects (Riley & Crooker 2004). More importantly, even under such idealized conditions, the flux rope develops consiserable structure, suggesting that interpreting and de-convolving STEREO observations of the same ICME will be a challenge. We also note the presence of outflow associated with post-eruption reconnection underneath the flux rope, which has remained intact within the expansion wave (rarefaction region) behind the flux rope; It has a limited latitudinal extent ($\pm 15°$) and trails the ejecta by $\approx 35 R_\odot$ at

1 AU (middle panel). This aspect of the simulation is discussed in more detail by Riley et al. (2002b).

A comparison of different techniques that fit the magnetic structure of an ICME to force-free and non-force free flux ropes was performed by Riley et al. (2004). Such end-to-end models of the Sun-to-Earth system are of course extremely important to provide a self-consistent context for modeling the STEREO multipoint images and multipoint in-situ SEP measurements.

5.2. MODELING OF EUV EMISSION OF CMES

The field of view of the SECCHI/EUVI imager extends to about 1.7 $R_\odot$, so EUV emission of CMEs can only be imaged in the corona during the first few minutes after their launch, while the propagation further out can be tracked in white light with SECCHI/COR (COR1: 1.1-3.0 $R_\odot$; COR2: 2-15 $R_\odot$) and SECCHI/HI (12-318 $R_\odot$). The 3D reconstruction of CMEs in EUV can be approached in two different ways: either with forward-fitting using a parameterized 3D density model $n_e(x,y,z,t,T)$, or by "tomographic" inversion (e.g., using a back-projection method). The first method can be very computing intensive if there is a large number of free parameters involved, while the second method suffers from extreme undersampling in the case of two spacecraft only (though an additional third view might be available from the SoHO/EIT telescope).

Although no efficient method has been published yet for the 3D reconstruction of CMEs from stereoscopic EUV images, we expect that some iterative forward-fitting method will be developed in near future that has a feedback between the goodness of the fit and the variation of the free model parameters. Once a geometric density model is specified for a given time t, i.e., $n_e(x,y,z,T)$, the EUV intensity for an optically thin spectral line of wavelength λ_{ij} (for transition from atomic energy level ε_j to a lower level ε_i) for a given line-of-sight in direction z is then

$$I(\lambda_{ij}) = A_X \int C(T,\lambda_{ij},n_e)\; n_e n_H \; dz \;, \tag{1}$$

where $A_X = N(X)/N(H)$ is the abundance factor of element X to hydrogen H, n_e the electron density, n_H the hydrogen density, and $C(T,\lambda_{ij},n_e)$ is the *contribution function*,

$$C(T,\lambda_{ij},n_e) = \frac{h\nu_{ij}}{4\pi}\frac{A_{ji}}{n_e}\frac{N_j(X^{+m})}{N(X^{+m})}\frac{N(X^{+m})}{N(X)} \qquad (\mathrm{erg\ cm^{-2}\ s^{-1}\ ster^{-1}}) \;, \tag{2}$$

with $N_j(X^{+m})$ the population number of the ionization state $+m$. Since the corona is fully ionized, we can use the so-called *coronal approximation* by setting the hydrogen density equal to the electron density, $n_H \approx n_e$, which demonstrates that the (optically thin) EUV emission is essentially proportional to the squared electron density, $I \propto n_e^2$, for a given temperature T. For the calculation of the contribution function $C(T,\lambda_{ij},n_e)$, there are now codes available in the solar community,

e.g., the CHIANTI code (Dere et al. 1997, 2001; Young et al. 1998; Landi et al. 1999; see also URL site in Table 2). The total density function at any point in a CME can then be obtained (at time t) by integrating over all temperatures, $n_e(x,y,z,t) = \int n_e(x,y,z,t,T)dT$. If we manage to come up with an approximate (time-dependent) density model $n_e(x,y,z,t)$ from modeling the stereoscopic EUV images, either by forward-fitting or by inversion, we can then use this model as input or test comparison for dynamic CME models simulated with 3D MHD codes (§5.1).

5.3. MODELING OF WHITE-LIGHT EMISSION OF CMES

The SECCHI/COR1, COR2, and HI instruments will track CMEs in white light over a range from 1.1 $R_\odot$ to 328 $R_\odot$ (≈ 1.5 AU), so they are the primary imagers for 3D reconstruction of propagating CMEs. 3D reconstruction and visualization of CMEs in white light is mostly led by the *Naval Research Laboratory (NRL)* and *Max Planck Institut für Sonnenforschung (MPS)* Teams. The goal is to reconstruct the 3D density distribution $n_e(x,y,z,t)$ in the solar K-corona, such as polar plumes, equatorial streamers, and CMEs. Information is available in total *brightness (B)* images as well as in *polarized brightness (pB)* images. Standard tomographic methods are not suitable for only two projections. Maximum entropy and pixon methods (Puetter 1995, 1996, 1997; Puetter & Yahil 1999) are considered as more viable, currently investigated by the NRL Team. Current tests with a pixon code require relatively long computing times, but demonstrate successful reconstructions of simple CME geometries (e.g., cones or semi-shells).

In order to reconstruct the electron density from the image of the K-corona captured by the spacecraft, we have to integrate the *Thomson-scattered* light from all directions that are incident on the spacecraft. The scattered radiation can be separated into tangentially and radially polarized light. The *tangential emission coefficient* ε_t may be written as (Billings 1966),

$$\varepsilon_t(\mathbf{r}) = \frac{\pi I_0 \sigma}{2} n_e(\mathbf{r}) \Sigma_A \qquad (\text{photons s}^{-1}) \,, \tag{3}$$

and the *radial emission coefficient* ε_r may be written as

$$\varepsilon_r(\mathbf{r}) = \frac{\pi I_0 \sigma}{2} n_e(\mathbf{r}) [\Sigma_B \cos^2(\chi_s) + \Sigma_C] \qquad (\text{photons s}^{-1}) \,. \tag{4}$$

I_0 is the solar intensity at disk center, R is the solar radius, r is the distance of the scattering point from Sun center, σ is the Thomson scattering cross section, χ_s is the scattering angle, and Σ_A, Σ_B, and Σ_C, are functions of r/R which account for the non-zero radius of a limb-darkened Sun (Billings 1966; Minnaert 1930; Milne 1921; Neckel & Labs 1994). Note that there are two important differences to EUV imaging: (1) white light emission is proportional to the total density, while EUV emission is proportional to the squared density, and (2) white light sees the total

density summed over all temperatures, while EUV images see only the density in the temperature range of a particular filter. Simulations of white-light images from model 3D density distributions are visualized in Lugaz et al. (2005) and in Pizzo & Biesecker (2004). The latter study demonstrates a robust triangulation method to obtain the centroid location, approximate shape, and velocity of CMEs, using a sequence of stereoscopic white-light images. Some new insight about the 3D configuration of CME shapes is also obtained from a recent data analysis study by Cremades & Bothmer (2004), which shows that CMEs arise in a self-similar manner from pre-existing small-scale loop systems, overlying regions of opposite magnetic polarities, which can be exploited to predict some geometric properties based on the relative orientation of the underlying neutral line in each hemisphere.

Based on the density determination of CMEs from white-light images, the total mass and velocity of a CME can be quantified during propagation, which allows to study the energetic balance between potential, kinetic, and magnetic energy, whose sum is found to approximately conserved based on LASCO data (Vourlidas et al. 2000).

A complementary method of 3D reconstruction of CMEs in white light is the method of 3D polarimetric imaging (Moran & Davila 2004; Dere et al. 2005). The underlying assumption in this method is that the polarized brightness increases for Thomson scattering with $I_p \propto sin^2\chi$, while the unpolarized brightness decreases with increasing $sin^2\chi$. This information can be used to distribute the mass $n_e(x,y,z)$ along each line-of-sight z in such a way that it matches both the polarized brightness $pB(x,y)$ and unpolarized brightness $B(x,y)$. Although this method can be used for a single white-light imager (e.g., as demonstrated for SoHO/LASCO), it promises an even better constrained 3D reconstruction for two stereoscopic spacecraft, and thus will provide a very useful test for alternative reconstruction methods (such as pixon).

Further out in the heliosphere, the 3D density distribution of CMEs can be reconstructed tomographically either from polarized brightness data or from interplanetary scintillation (IPS) data (Jackson & Froehling 1995; Jackson & Hick 2002, 2004), as mentioned in §3.2 (Fig. 6).

5.4. Modeling of Radio Emission of CMEs

Although there is no radio imaging capability onboard the STEREO spacecraft, we emphasize that ground-based radio imaging can provide a very useful complement for 3D reconstructions of CMEs. In the CME event of 1998-Apr-20 it was demonstrated for the first time that an expanding CME can be imaged directly at (metric) radio wavelengths, based on the nonthermal synchrotron emission from electrons with energies of $\approx 0.5-5$ MeV (Bastian et al. 2001). CMEs might even be imaged in radio wavelengths based on their thermal free-free emission (Gopalswamy & Kundu 1993; Bastian & Gary 1997), which would help to constrain their 3D density and temperature distribution. Joint radio imaging (with the Nançay ra-

dioheliograph) and SoHO/LASCO observations of a CME indicate also successive magnetic reconnection events at the CME leading edge that are responsible for multiple injections of electrons into interplanetary space (Pick et al. 1998).

6. Modeling of Interplanetary Shocks

6.1. MHD Modeling of Interplanetary Shocks

CMEs have typical propagation speeds of $v \approx 300 - 400$ km s^{-1}, but fast CMEs have been measured in excess of $v = 2000$ km s^{-1}. The *fast solar wind* has a typical speed of $v \approx 800$ km s^{-1}. The fast-mode speed dictates whether a fast-mode shock will form, leading to CME-driven transient interplanetary shocks. Numerical simulations with HD or MHD codes (e.g., Fig. 15), have been able to reproduce the observed speeds and pressure profiles of shocks and CME events out to large distances from the Sun. In such simulations, a pressure pulse is initiated in the lower corona. As the front of a fast CME overtakes the slower solar wind, a strong gradient develops and pressure waves steepen into a forward shock propagating into the ambient wind ahead, and occasionally a reverse shock propagates back through the CME towards the Sun. Numerical simulations of CMEs propagating from the corona (Mikić & Linker 1994; Linker & Mikić 1995; Linker et al. 2001) through the heliosphere can be found in Odstrčil et al. (1996, 2002), Odstrčil & Pizzo (1999a,b,c), and Odstrčil, Pizzo, & Arge (2005). The shock strength as well as the stand-off distance between the shock front and the CME driver gas can vary considerably across the structure, depending where compression or rarefaction occurs between the slow solar wind in the streamer belt and the fast solar wind in coronal holes (Odstrčil & Pizzo 1999b,c). The predicted arrival time of CME shocks at 1 AU depends critically on the modeling of the background solar wind, which controls the shock propagation speed (Odstrčil, Pizzo, & Arge 2005).

There are a number of complications that can occur, such as the fact that a faster CME can catch up with a slower CME and interact (Gopalswamy et al. 2001). Such interactions form compound streams in the inner heliosphere. These systems continually evolve further and merge with other CMEs and shocks as they move outward. In the outer heliosphere, beyond 5 AU, such structures form *Global Merged Interaction Regions (GMIRs)*, which become so extensive that they encircle the Sun like a distant belt. Such regions block and modulate galactic cosmic rays (i.e., the flux of high-energy particles that continuously streams into the heliosphere). Finally, a forward interplanetary shock wave that passes the Earth's magnetosphere may cause a sudden commencement of a *magnetic storm* or *substorm* at the Earth and change the electrical and magnetic connection of the interplanetary magnetic field with the Earth's magnetic field.

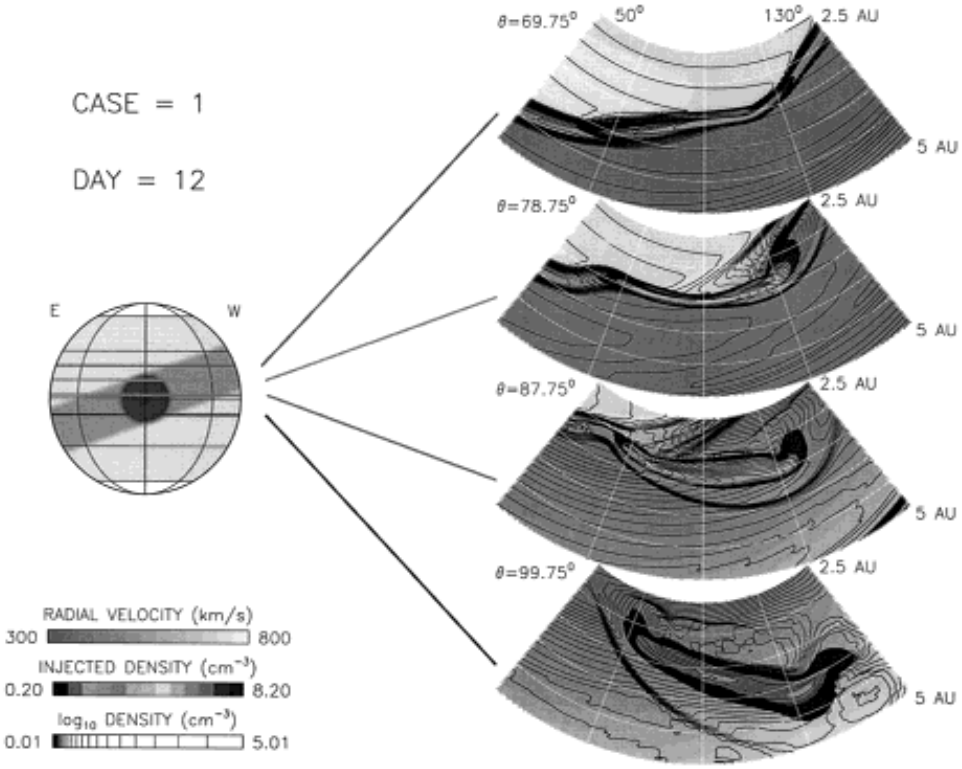

Figure 15. Numerical MHD simulations of a CME shock wave moving through the ambient solar wind. The CME is injected in the center of the heliospheric current sheet streamer belt (left), which is tilted to the solar axis. The propagating CME is shown at slices in heliographic longitudes and at a distance of 2.5-5 AU from the Sun 12 days after launch. The slices are 4 different heliographic latitudes and show how the CME's shape, pressure and speed vary depending on the ambient solar wind conditions (Courtesy of Victor Pizzo).

6.2. DETECTION OF INTERPLANETARY SHOCKS BY STEREO

The kinematic 3D reconstruction of a CME leading edge with SECCHI/COR and HI will provide the true 3D velocity $\mathbf{v}(\mathbf{r})$ of the propagating shock front, while previous measurements with a single spacecraft (e.g., with SoHO/LASCO) yielded only the velocity component projected in the plane-of-sky, and thus only a lower limit. A large number of CMEs will therefore reveal a higher propagation speed than previously reported values, which may also give a systematic correction from subsonic to supersonic propagation speeds. Triangulation measurements with SECCHI will therefore be an important diagnostic of the true Mach number of interplanetary shocks.

The double-spacecraft configuration of STEREO will also provide situations where a CME shock passes one spacecraft, while the other can observe the CME shock from the side. This provides a unique opportunity to relate the in-situ mea-

surements of shock-accelerated or shock-trapped particles at one spacecraft to the density and velocity diagnostic from the other spacecraft. Specific modeling of such situations has not been published so far, but we anticipate that such data analysis will provide insights into shock acceleration, the primary shock structure, its interactions with corotating streams, interaction regions (CIRs), secondary interplanetary shocks, and transient (solar wind) flows. Detection of radio waves from shock-associated particle beams and energetic particles (SEPs) will be discussed in more detail in the next two sections (§7, 8).

7. Modeling of Interplanetary Particle Beams and Radio Emission

7.1. Particle Beams and Radio Type III Emission

Particle beams, i.e., nonthermal particles with an anisotropic velocity distribution concentrated in parallel direction to the magnetic field, reveal flare-associated or CME-associated acceleration processes. Flares can produce interplanetary particle beams if the coronal magnetic reconnection site is connected with interplanetary space via open magnetic field lines. Alternatively, interplanetary particle beams might be generated in situ in interplanetary super-Alfvénic CME shock waves. So, the localization and tracking of these dual sources of interplanetary particle beams will be a fitting task for the STEREO mission.

Since the plasma in interplanetary space is collisionless, superthermal and high-energy particles can propagate through interplanetary space and form particle beams (e.g., electron beams or ion beams). The velocity dispersion causes the higher energy electrons to stream ahead of the lower energy electrons, creating a transient bump-in-tail instability. The free (kinetic) beam energy is converted into Langmuir waves via the Landau resonance, and some Langmuir wave energy is converted into radio waves at the fundamental or harmonic local plasma frequency (e.g., McLean & Labrum 1985). Thus, beam-driven type III-like radio bursts are common in interplanetary space. The spatial size of interplanetary radio bursts can be very large, since the extent of the radio source grows with distance from the Sun. A quantitative model of interplanetary type III emission, which incorporates large-angle scattering and reabsorption of fundamental emission amid ambient density flucutations, called *stochastic growth theory*, accounts for anomalous harmonic ratios, the exponential decay constant of bursts, burst rise times, and the directivity of type III emission (Robinson & Cairns 1998a,b,c), which is suitable for comparisons with SWAVES and IMPACT measurements.

7.2. Shock Waves and Radio Type II Emission

A classic radio diagnostic of propagating shock fronts are type II bursts, which is plasma emission at the fundamental and harmonic plasma frequency generated in coronal and interplanetary shocks, appearing as slowly-drifting pair bands in radio

dynamic spectra. Type II bursts are interpreted in terms of shock waves, either CME-driven or blast waves, that accelerate electrons and produce radio emission near the electron plasma frequency f_{pe} and near $2f_{pe}$ in the upstream region (Wild et al. 1963; Nelson & Melrose, 1985; Bale et al. 1999; Cairns & Kaiser 2002; Warmuth & Mann, 2005). However, there is not a one-to-one correspondence between the existence of shocks and type II bursts. Slowly-drifting type II bursts mark the passage of a shock, but not all shocks produce radio bursts. Furthermore, type II bursts do not outline the entire shock front, but occur only where a shock wave intersects preexisting structures (Stewart 1984; Reiner & Kaiser 1999). However, interplanetary type II bursts were all found to be associated with fast CMEs, with shock transit speeds $\gtrsim 500$ km s^{-1} (Cane, Sheeley, & Howard 1987).

Dynamic spectra of both coronal and interplanetary type II bursts routinely show multiple emission bands that appear and disappear, have different frequencies and frequency drift rates, and time varying intensities (e.g., Reiner et al. 1998a; Cane & Erickson 2005). One goal of the two STEREO/SWAVES instruments is to remotely track type II bursts and interpret the varying frequency fine structures in terms of emission from spatially distinct regions of the shock as they move through the inhomogeneous solar wind. This inversion requires detailed theoretical modelling of type II emission. Recent MHD simulations of CME shocks show also that a single flare/CME event can generate coronal disturbances observed as two separate type II radio bursts (Odstrčil & Karlický 2000).

A semi-quantitative theory exists for type II bursts (Knock et al. 2001, 2003a,b; Knock & Cairns, 2005), which combines (i) "magnetic mirror" reflection and acceleration of upstream electrons incident on the shock, using magnetic moment conservation in the *de Hoffman-Teller frame*, (ii) formation of foreshock electron beams by "time-of-flight" effects, using Liouville's theorem, (iii) estimation of the net energy flow Langmuir waves driven by the electron beams, using quasilinear relaxation and stochastic growth theory, (iv) conversion of Langmuir energy into radiation near f_{pe} and $2f_{pe}$, using nonlinear Langmuir wave processes with known conversion efficiencies, with shock propagation through an inhomogeneous solar wind. Fig. 16 shows the dynamic spectrum predicted for a shock moving through an MHD Parker-model solar wind with 2 corotating interaction regions (CIRs), two magnetic clouds (e.g., associated with CMEs), and random small-scale inhomogeneities in plasma quantities like density, flow speed, and vector magnetic field (Knock & Cairns 2005). Features associated with the shock's interactions with specific CIRs and clouds are identified (cf., Reiner & Kaiser 1999; Gopalswamy et al. 2001), while the smaller time scale variations are due to the random solar wind turbulence leading to enhanced or decreased emission from localized regions of the shock. Moreover, predictions for multiple observers show considerable differences interpretable in terms of proximity and frequency-blocking effects, directly relevant to future interpretations of STEREO data. The type II burst model of Knock & Cairns (2005) reproduce a number of observed features that can be used for more detailed diagnostic of the underlying shocks. For instance, the intensity of type II

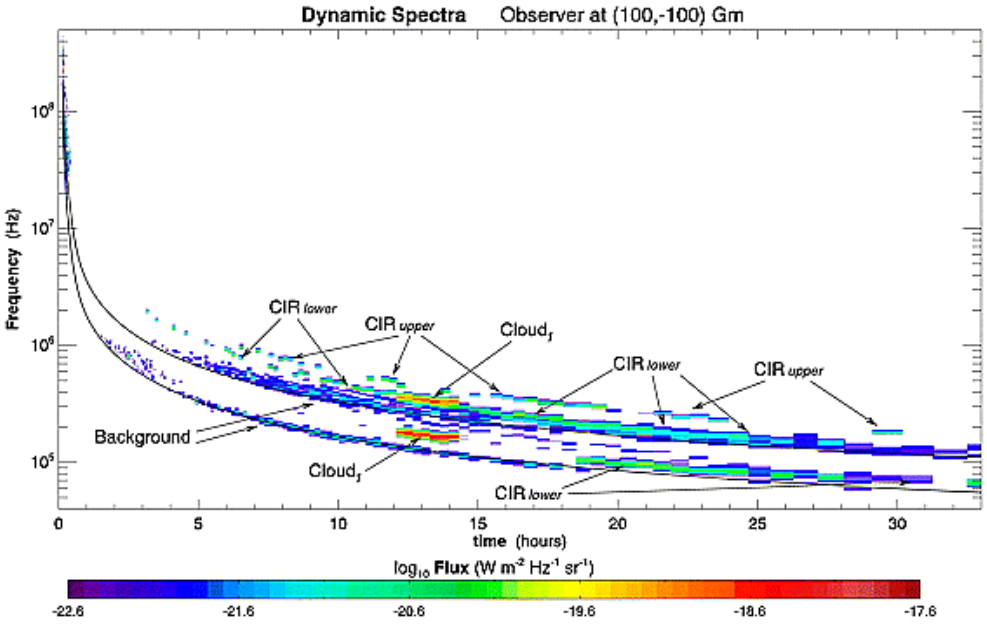

Figure 16. Dynamic spectrum of a type II burst. The two solid curves are the fundamental and harmonic frequency drift rate of the shock's leading edge. The structures responsible for various spectral features are indicated (Knock & Cairns 2005).

bursts is strongly diminished near a peak in the heliospheric Alfvén speed profile. Other features observed in dynamic spectra of type II bursts, such as multiple-lane effects, variations in the frequency-time drift rate $d\nu/dt$, onsets and turn-offs of emission, narrowband and broadband emission, can be reproduced with this type II model by inserting local structures in the coronal or interplanetary plasma.

It is envisaged that the microscopic physics of this and other theories will be tested and improved using future IMPACT and SWAVES data, extended to include macroscopic shock and solar wind models and directivity effects, and used to interpret STEREO white light and radio data in terms of CMEs, shocks, and other interplanetary structures. For a full understanding of the link between CMEs and type II bursts, knowledge on strong interplanetary shocks, the macroscopic and microscopic structure of CME-driven shocks, the generation mechanism of radio emission, and the radiation beaming pattern are required.

7.3. MODELING FOR STEREO/WAVES

Interplanetary radio bursts provide a rich diagnostic on the acceleration and propagation of energetic particles and shock waves (Fig. 17). Radio bursts with plasma frequencies $\gtrsim 20$ MHz (above the Earth's ionospheric cutoff frequency) can be observed with ground-based radio telescopes, which extends only out to about 1-2 solar radii, while all interplanetary radio bursts further out have lower plasma

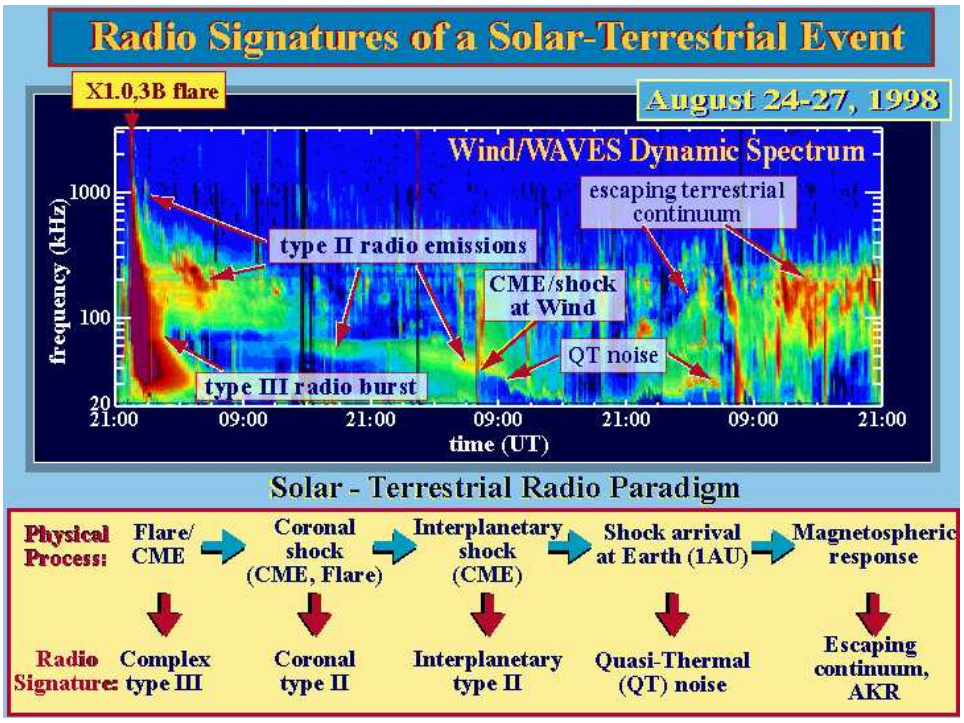

Figure 17. Overview of physical processes and corresponding radio signatures produced by a flare/CME event. The radio dynamic spectrum is observed by the WIND spacecraft for the 1998 Aug 24-27 geoeffective event (SWAVES website).

frequencies and require space-based radio detectors such as STEREO/SWAVES. Previous stereoscopic radio experiments (STEREO-1) with a single spacecraft and a ground-based instrument were able to map out the directivity pattern of type III bursts (Caroubalos & Steinberg 1974; Caroubalos, Poquerusse, & Steinberg 1974; Reiner & Stone 1986, 1988, 1989), while a combination of three spacecraft was able to resolve the 3D trajectory of type III bursts and to demonstrate harmonic emission (Gurnett et al. 1978; Reiner et al. 1998b; Dulk et al. 1985).

The *STEREO/WAVES (SWAVES)* instruments will have two vantage points in space, and can also be combined with a third viewpoint from ground (at least for frequencies $\gtrsim 20$ MHz). SWAVES will be able to triangulate type II and type III radio emission and can observe them remotely as well as in situ together with associated plasma waves, while IMPACT and PLASTIC instruments can detect radio-associated nonthermal particles in situ. The two-point wave measurements by the two identical SWAVES instrument (combined with the particle detections by IMPACT and PLASTIC) can map out the acceleration efficiency and conversion efficiency into radio waves at two geometrically different parts of a shock, for instance in parallel shock regions (at the CME front) and in perpendicular shock regions (in the flanks of a CME), for large stereoscopic separation angles later in the

mission. Previous measurements showed that type II emission upstream of a strong CME-driven interplanetary shock is strongest in quasi-perpendicular shock regions (Bale et al. 1999). The triangulation of the strongest radio type II source as function of time will track the location of most efficient particle acceleration and conversion into radio emission within a propagating shock front. The triangulation of multiple radio sources will reveal the detailed shock structure (e.g., foreshock regions). Furthermore, since SWAVES can triangulate the absolute position of plasma emission sources, the plasma frequency and related electron density $n_e(\mathbf{r})$ can be determined directly without using heliospheric density models. The triangulated radio source will also yield the direct radial speed $\mathrm{v}(\mathbf{r})$ of the CME-driven shock from the Sun to 1 AU, providing real-time predictions of the shock arrival at Earth.

8. Modeling of Solar Energetic Particles (SEPs)

Solar energetic particle (SEP) events refer to accelerated high-energy particles detected in the heliosphere. Some originate in solar flares, while others are accelerated in transient interplanetary shocks, as they are produced by fast CMEs. The acceleration mechanisms can be DC electric fields, stochastic wave-particle interactions, or shock acceleration mechanisms. Solar energetic particle events are classified into two types, *gradual* and *impulsive* SEP events, depending on their energy versus time profile. *Gradual SEP events* occur with a rate of ≈ 10/year during the maximum of the solar cycle, each one can last several days, and they are likely to be accelerated directly in interplanetary shocks rather than by flares in the corona. *Impulsive SEP events* occur more frequently, with a rate of ≈ 100/year during the maximum of the solar cycle, they last only a few hours, and they are much weaker than gradual SEP events. Since they originate along magnetic field lines connected to coronal flare sites, their acceleration could be governed by the same magnetic reconnection processes that governs the associated flare. So, charged particles can be used to trace the interplanetary field topology (Kahler 1997).

Because the ^{3}He/^{4}He ratio of SEPs is much higher than in the normal solar wind, they are also called ^{3}He-rich events. Interplanetary particles can also be accelerated in the electric fields that are generated at corotating interaction regions (CIR) between high-speed and low-speed streams. The location where acceleration of interplanetary particles takes place can approximately be determined from the velocity dispersion (i.e., time-of-flight effects), $t_{prop} = L/\mathrm{v}$, of particles arriving at Earth. Multi-spacecraft observations help us to map the spatial distributions of the accelerated particles that flow out into the heliosphere from the evolving CME shock or those that remain trapped behind it (Reames 1997). Particularly advantageous opportunities are in-situ particle observations in CME fronts that are observed in *Earth-STEREO-Sun quadrature configuration* (Fig. 18), i.e., when the CME is observed from the side (rather than head-on as with SoHO previously).

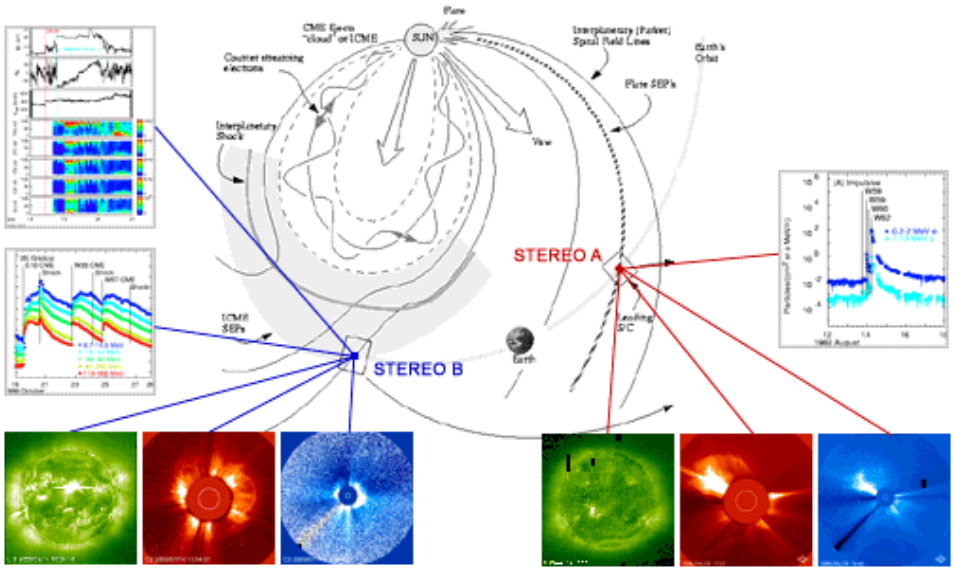

Figure 18. Possible STEREO/IMPACT observations of SEPs at two magnetically disconnected locations in the heliosphere: STEREO-A is located on an open magnetic field line that is connected to the coronal flare region and will probe flare-accelerated particles, while STEREO-B probes SEPs in-situ in a CME-driven shock in interplanetary space at 1 AU (IMPACT website).

Such quadrature observations should reveal the shock profile more clearly than at other viewing angles.

8.1. THEORETICAL MODELING OF SEP ACCELERATION

The most recent theoretical modeling of SEP acceleration includes coupled hydromagnetic wave excitation and ion acceleration in an evolving coronal/interplanetary shock (Lee 2005), the injection problem at an CME-driven shock (Zank & Li 2004), or SEP acceleration in solar wind compression regions associated with CIRs (Giacalone, Jokipii, & Kóta 2002). The acceleration of solar energetic particles (SEPs) at an evolving coronal/interplanetary CME-driven shock is the most promising theory for the origin of SEPs observed in the large gradual events associated with CMEs (Lee 2005). This calculation includes the essential features of the process: diffusive shock acceleration, proton-excited waves upstream of the shock, and escape of particles upstream of the shock by magnetic focusing. The wave spectra and particle distributions predicted are in general agreement with observations but improvement is needed including the form of the excited wave spectrum, which affects ion fractionation and the form of the high-energy cutoff, and a more general velocity distribution for the injected seed population. The seed populations for quasi-perpendicular and quasi-parallel shocks are subjects of current debates. One thought is that quasi-parallel shocks generally draw their seeds from solar-wind suprathermals, while quasi-perpendicular shocks – requiring a higher initial

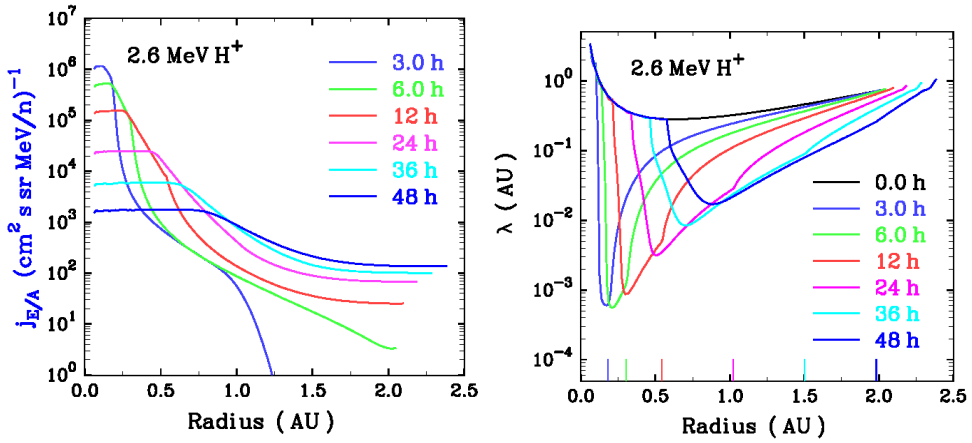

Figure 19. Coupled evolution of 2.6 MeV proton intensity (left) and mean free path (right) versus radius (Ng, Reames, & Tylka 2003).

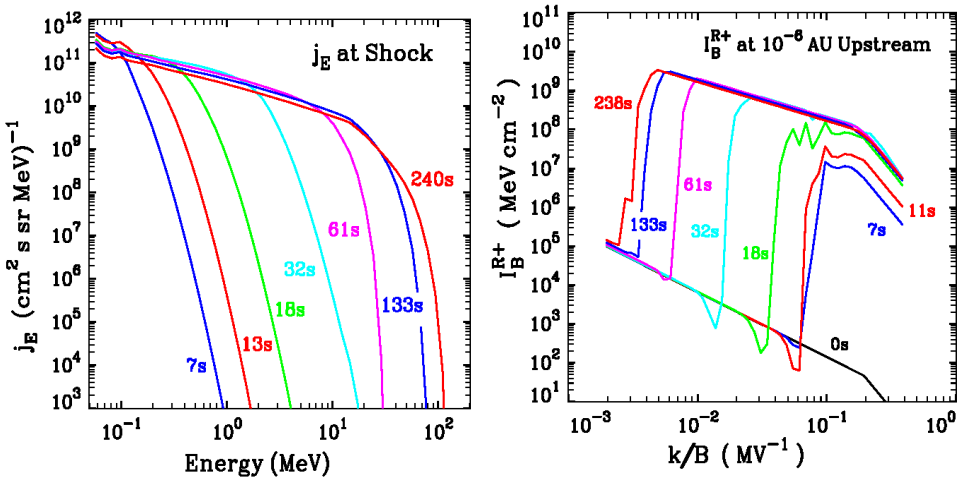

Figure 20. Proton acceleration (left) and Alfvèn wave growth (right) upstream of a moving shock at $\sim$ 3.7 solar radii (Courtesy of Chee Ng and Don Reames).

speed for effective injection – preferentially accelerate seed particles from flares. These different origins of seed populations can explain the observed differences in the composition of high-energy SEPs (Tylka et al. 2005).

Numerical modeling of SEP acceleration is now approached by combining MHD fluid codes with kinetic codes, to obtain a self-consistent description of CME shocks and SEP acceleration. In a recent study SEP particles are accelerated in a CME-driven shock at $5R_{\odot}$ when the shock exceeds a fast-mode Mach number of $\gtrsim 4$, producing solar energetic protons with energies below 10 GeV, for which a cutoff energy of ≈ 10 GeV would be predicted by diffusive shock acceleration (Sokolov et al. 2004; Roussev et al. 2004).

8.2. MODELING OF SEP FOR STEREO/IMPACT

STEREO/IMPACT will sample the 3D distributions of SEP ions and electrons, as well as the local magnetic field (Fig. 18). SEP modeling with specific relevance for IMPACT is described in Ng, Reames, & Tylka (1999, 2003). This line of SEP modeling focuses separately on SEP transport over several AU and their extension to fast acceleration by a coronal shock on fine time and spatial scales. Both efforts study the coupled nonlinear evolution of SEPs and Alfvén waves in inhomogeneous plasma and magnetic field, featuring self-consistent quasilinear wave-particle interaction with full pitch-angle dependence. Both models include focusing, convection, adiabatic deceleration, and scattering (by Alfvén waves) for SEPs, and wave transport and amplification (by SEPs) for the Alfvén waves. The acceleration model treats, in addition, first-order Fermi acceleration and wave transmission/reflection at the shock. The results reveal that, contrary to common assumption, wave amplification strongly impacts SEP acceleration and transport. This transport model predicts the self-throttling of proton transport through wave excitation (Ng, Reames & Tylka 2003), as shown by the evolution of the radial profiles of SEP intensity j_E and mean free path λ (Fig. 19). Wave growth also explains the observed complex time variations of SEP elemental abundances (Tylka, Reames, & Ng 1999). The shock acceleration model predicts proton intensity and Alfvén wave spectra evolving in tandem upstream of a 1800 km/s shock traveling from 3.7 to 4.3 solar radii (Fig. 20). Acceleration of 1 MeV (70 MeV) protons "ignites" at 18 s (130 s), when wave growth drives the respective λ down from 0.5 AU (1 AU) to below 10^{-4} AU. Future work will attempt to integrate the shock acceleration and interplanetary transport models and to generalize it so that it can accept arbitrary input of plasma and shock parameters from other CME and shock models.

Attempts are being made to add SEPs to the Sun-to-Earth end-to-end MHD models at CCMC, CISM, and University of Michigan, which simulate SEP acceleration in realistic CME environments (e.g., Roussev et al. 2004). The STEREO multipoint measurements and multiple viewpoints of the SEP sources will be combined with the models to answer outstanding questions like the relative contribution of flare versus IP shock-generated SEPs in major events. Both the Michigan group and the CISM group are attempting these end-to-end system models, and CCMC has the role of a model component provider to STEREO and the larger community.

9. Modeling of Geoeffective Events and Space Weather

A key requirement in evaluating geoeffective events and space weather is the determination of CME trajectories towards Earth, with the goal to establish magnetic connectivity and to predict the timing and impact of CME-induced geomagnetic disturbances. While previous single-spacecraft observations (e.g., with SoHO/LASCO) have difficulty in reconstructing the directionality of CMEs, in

particular for *frontside halo CMEs*, the dual vantage point of the two STEREO spacecraft will provide unambiguous directionality measurements and better arrival forecasts (in real time) from the true 3D vector $\mathbf{r}(t)$ and velocity $\mathbf{v}(t)$ reconstructions by the SECCHI/HI imagers. Once the Sun-Earth connectivity of the CME path is established, we further want to know whether the CME hits the Earth directly, grazes it, or misses it, what the longitudinal extent and cross-section of a CME is, and what the southward magnetic field component B_z is (which determines the geoeffectiveness).

Current modeling efforts of space weather are coordinated by Dave Webb (see chapter on Space Weather and Beacon mode) and by Jim Klimchuk at NRL. MHD Modeling for the ESA Space Weather Initiative is coordinated by David Berghmans. An effort to model the geoeffectiveness of CMEs is planned by the 3D reconstruction group led by Volker Bothmer. Modeling of the magnetic field that connects the subphotospheric domain with the coronal magentic field during CME initiation is also addressed by the *Solar Multidisciplinary University Research Initiative (SOLAR/MURI)* at the *University of California, Berkeley (UCB)*. Particular efforts to model space weather by end-to-end simulations of CMEs and SEPs are ongoing at the *Center for Integrated Space Weather Modeling (CISM)* at the *University of California at Berkeley (UCB)*, and at the *Center for Space Environment Modeling (CSEM)* at the University of Michigan, which we partly described in Section 3.2 on heliospheric solar wind models. Their *Space Weather Modeling Framework (SWMF)* aims to come up with a self-consistent framework of models that starts from the CME initiation in the solar corona, follows the CME propagation and SEP acceleration through interplanetary space, and predicts the consequences in the Earth's magnetosphere. Part of their space weather modeling includes also predictions of fluxes and arrival times of high-energy protons at spacecraft locations, which produce a real radiation hazards for manned and unmanned spacecraft. More information of the activities of various groups that perform space weather modeling relevant for the STEREO mission can also be found from the URLs given in Table 2.

Acknowledgements

Part of the work was supported by NASA contract N00173-01-C-6001 and N00173-02-C-2035 to NRL (SECCHI project).

TABLE II

Acronyms and URLs of webpages relevant to modeling of STEREO data.

Acronym	Full Name ↦ *Website URL*
CACTUS	Computer Aided CME Tracking ↦ *http://sidc.oma.be/cactus/*
CCMC	The Community Coordinated Modeling Center ↦ *http://ccmc.gsfc.nasa.gov/*
CHIANTI	Atomic Database for Spectroscopic Diagnostics of Astrophysical Plasmas ↦ *http://wwwsolar.nrl.navy.mil/chianti.html/*
CISM	Center for Integrated Space Weather Modeling ↦ *http://sprg.ssl.berkeley.edu:80/cism/*
CSEM	Center for Space Environment Modeling ↦ *http://csem.engin.umich.edu/*
IMPACT	In-situ Measurements of Particles and CME Transients ↦ *http://sprg.ssl.berkeley.edu/impact/*
PLASTIC	PLastic And SupraThermal Ion Composition investigation ↦ *http://stereo.sr.unh.edu/*
SECCHI	Sun Earth Connection Coronal and Heliospheric Investigation ↦ *http://stereo.nrl.navy.mil/*
SECCHI/MPS	The SECCHI website at Max Planck Institut für Sonnenforschung ↦ *http://star.mpae.gwdg.de/secchi/*
SMEI/UCSD	Solar Mass Ejection Imager, University California San Diego ↦ *http://cassfos02.ucsd.edu/solar/*
SOHO	SOlar and Heliospheric Observatory ↦ *http://sohowww.nascom.nasa.gov/*
SOLAR-B	SOLAR-B mission website ↦ *http://science.msfc.nasa.gov/ssl/pad/solar/solar-b.stm*
SOLAR/MURI	Solar Multidisciplinary University Research Initiative at UCB ↦ *http://solarmuri.ssl.berkeley.edu/*
STEREO	The Solar TErrestrial RElations Observatory (STEREO) ↦ *http://stereo.gsfc.nasa.gov/*
STEREO/SW	The STEREO Space Weather Group ↦ *http://stereo.nrl.navy.mil/swx/swindex.html*
SWAVES	The STEREO Waves Instrument ↦ *http://www-lep.gsfc.nasa.gov/swaves/swaves.html*
TRACE	Transition Region And Coronal Explorer ↦ *http://vestige.lmsal.com/TRACE/*

References

Alexander, D., Gary, G. A., & Thompson, B. J., 1998: 'Analysis of active regions via 3D rendering techniques', in *"Three-Dimensional Structure of Solar Active Regions"*, Proc. 2nd Advances in Solar Physics Euroconference, (eds. C.Alissandrakis & B.Schmieder), Astronomical Society of the Pacific (ASP), San Francisco, ASP Conference Series **155**, 100-104.

Altschuler, M. D. & Newkirk, G. Jr., 1969: 'Magnetic Fields and the Structure of the Solar Corona. I: Methods of Calculating Coronal Fields', *Solar Phys.*, **9**, 131-149.

Altschuler, M. D., Levine, R. H., Stix, M., & Harvey, J., 1977: 'High resolution mapping of the magnetic field of the solar corona', *Solar Phys.*, **51**, 345-375.

Altschuler, M. D., 1979: 'Reconstruction of the global-scale three-dimensional solar corona', in *"Image Reconstruction from Projections"*, (ed. G. T. Herman), Springer: Berlin, p.105-145.

Antiochos, S. K., DeVore, C. R., & Klimchuk, J. A. 1999: 'A model for solar coronal mass ejections', *ApJ*, **510**, 485-493.

Arge, C. N. & Pizzo, V. J., 2000: 'Improvement in the prediction of solar wind conditions using near-real time solar magnetic field updates', *JGR*, **105/A5**, 10,465-10,480.

Aschwanden, M. J. & Bastian, T. S., 1994a: 'VLA stereoscopy of solar active regions: I. Method and tests', *ApJ*, **426**, 425-433.

Aschwanden, M. J. & Bastian, T. S., 1994b: 'VLA stereoscopy of solar active regions: II. Altitudes, relative motion, and center-to-limb darkening of 20 cm emission', *ApJ*, **426**, 434-448.

Aschwanden, M. J., Lim, J., Gary, D. E., & Klimchuk, J. A., 1995: 'Solar rotation stereoscopy in microwaves', *ApJ*, **454**, 512-521.

Aschwanden, M. J. 1995: 'Imaging, Stereoscopy, and Tomography of the Solar Corona in Soft X-rays and Radio', *Lecture Notes in Physics*, **444**, 13-34.

Aschwanden, M. J., Newmark,J.S., Delaboudiniere,J.P., Neupert,W.M., Klimchuk, J. A., Gary, G. A., Portier-Fornazzi, F., & Zucker, A., 1999: 'Three-dimensional stereoscopic analysis of solar active region loops: I. SOHO/EIT observations at temperatures of 1.0-1.5 MK', *ApJ*, **515**, 842-867.

Aschwanden, M. J., Alexander, D., Hurlburt, N., Newmark, J. S., Neupert, W. M., Klimchuk, J. A., & Gary,G.A., 2000: '3D-Stereoscopic Analysis of Solar Active Region Loops: II. SOHO/EIT Observations at Temperatures of 1.5-2.5 MK', *ApJ*, **531**, 1129-1149.

Aschwanden, M. J., 2004: '*Physics of the Solar Corona - An Introduction*', Praxis Publishing Ltd., Chichester UK, and Springer, New York, ISBN 3-540-22321-5, 842p.

Aschwanden, M. J., Alexander, D., & DeRosa, M., 2004: 'Tomographic 3D-modeling of the solar corona with FASR', in *"Solar and Space Weather Radiophysics"*, Astrophysics and Space Science Library Vol. 314, (eds. D. E. Gary & C. O. Keller), Kluwer Academic Publishers, Dordrecht, The Netherlands, p.243-264.

Aschwanden, M. J., 2005: '2D Feature Recognition and 3D Reconstruction in Solar EUV Images', *Solar Phys.*, **228**, 341-360.

Bale, S. D., Reiner, M. J., Bougeret, J.-L., Kaiser, M. L., Krucker, S., Larson, D. E., & Lin, R. P., 1999: 'The source region of an interplanetary type II burst', *GRL*, **26/11**, 1573-1576.

Balogh, A., Marsden, R. G., & Smith, E. J. (eds.), 2001: *The Heliosphere Near Solar Minimum - The Ulysses perspective*, Springer-Praxis Books in Astrophysics and Astronomy, Praxis, Chichester, UK, and Springer, New York.

Bastian,T.S. & Gary,D.E., 1997: 'On the feasibility of imaging coronal mass ejections at radio wavelengths', *JGR*, **102/A7**, 14,031-14,040.

Bastian, T. S., Pick, M., Kerdraon, A., Maia, D., & Vourlidas, A., 2001: 'The Coronal Mass Ejection of 1998 April 20: Direct Imaging at Radio Wavelengths', *ApJ*, **558**, L65-L69.

Batchelor, D. A., 1994: 'Quasi-stereoscopic imaging of the solar X-ray corona', *Solar Phys.*, **155**, 57-61.

Berton, R. & Sakurai, T., 1985: 'Stereoscopic determination of the three-dimensional geometry of coronal magnetic loops', *Solar Phys.*, **96**, 93-111.

Billings, D. E., 1966: *'A Guide to the Solar Corona'*, Academic Press: New York.

Bothmer, V. & Schwenn, R., 1998: 'The structure and origin of magnetic clouds in the solar wind', *Ann.Geophysicae*, **16**, 1-24.

Bothmer, V., 2003: 'Sources of Magnetic Helicity Over the Solar Cycle', Proc. ISCS 2003 Symposium *"Solar Variability as an Input to the Earth's Environment"*, Tatranska Lomnica, Slovakia, 23-28 June 2003, ESA SP-535, 419-427.

Cairns, I. H., & Kaiser, M. L., 2002: 'The Review of Radio Science 1999-2002', *IEEE Press*, (eds. W.R.Stone), p.749.

Cane, H. V., Sheeley, N. R. Jr., & Howard, R. A., 1987: 'Energetic interplanetary shocks, radio emission, and coronal mass ejections', *JGR*, **92**, 9869-9874.

Cane, H. V., & Erickson, W. C., 2005: 'Solar Type II Radio Bursts and Interplanetary Type II Events', *ApJ*, **623**, 1180-1194.

Caroubalos, C. & Steinberg, J.-L., 1974: 'Evidence of solar bursts directivity at 169 MHz from simultaneous ground based and deep space observations (STEREO-1 Preliminary Results)', *A&A*, **32**, 245-254.

Caroubalos, C., Poquerusse, M., & Steinberg, J.-L., 1974: 'The directivity of type III bursts', *A&A*, **32**, 255-267.

Chen, J., Howard, R. A., Brueckner, G. E., Santoro, R., Krall, J., Paswaters, S. E., St.Cyr, O. C., Schwenn, R., Lamy, P., & Simnett, G. M., 1997: 'Evidence of an erupting magnetic flux rope: LASCO coronal mass ejection of 1997 April 13', *ApJ*, **409**, L191-L194.

Chen, J., Santoro, R. A., Krall, J., Howard, R. A., Duffin, R., Moses, J. D., Brueckner, G. E., Darnell, J. A., & Burkepile,J.T., 2000: 'Magnetic geometry and dynamics of the fast coronal mass ejection of 1997 September 9', *ApJ*, **533**, 481-500.

Chen, P. F., Wu, S. T., Shibata, K., & Fang, C., 2002: 'Evidence of EIT and Moreton Waves in Numerical Simulations', *ApJ*, **572**, L99-L102.

Cremades, H. & Bothmer, V., 2004: 'On the three-dimensional configuration of Coronal Mass Ejections', *A&A*, **422**, 307-322.

Davila, J. M., 1994: 'Solar tomography', *ApJ*, **423**, 871-877.

Davila, J. M., Rust, D. M., Pizzo, V. J., & Paulett, C., 1996: 'Solar Terrestrial Relations Observatory (STEREO)', (SPIE Proc. "Missions to the Sun", ed. D. M. Rust) *SPIE*, **2804**, 34-38.

Davila, J. M. & St. Cyr, O., 2002: 'Science prospects for the STEREO mission', in Proc. 34th COSPAR Scientific Assembly, The Second World Space Congress, 2002 Oct 10-19, Houston, Texas, p.478.

Dere, K. P, Landi, E., Mason, H. E., Monsignori-Fossi, B. C., & Young, P. R., 1997: 'CHIANTI - An atomic database for emission lines', *A&A*, **125**, 149-173.

Dere, K. P., Landi, E., Young, P. R., & Del Zanna, G., 2001: 'CHIANTI - An Atomic Database for Emission Lines. IV. Extension to X-Ray Wavelengths', *ApJS*, **134**, 331-354.

Dere, K. P., Brueckner, G. E., Howard, R. A., Michels, D. J., & Delaboudiniere, J. P., 1999: 'LASCO and EIT observations of helical structure in coronal mass ejections', *ApJ*, **516**, 465-474.

Dulk, G. A., Steinberg, J. L., Lecacheux, A., Hoang, S., & MacDowall, R. J., 1985: 'On the visibility of type III radio bursts originating behind the sun', *A&A*, **150**, L28-L30.

Forbes, T. G., 2000: 'A review on the genesis of coronal mass ejections', *JGR*, **105/A10**, 23,153-23,166.

Foullon, C., 2003: 'Automated detection and 3D reconstruction of EUV prominences', in Proc. ISCS Symposium on *"Solar Variability ans an Input to the Earth's Environment"*, (ed. A. Wilson), ESA, ESTEC Noordwijk, The Netherlands, (in press).

Frazin, R. A., 2000: 'Tomography of the solar corona I. A robust, regularized, positive estimation method', *ApJ*, **530**, 1026-1035.

Frazin, R. A. & Janzen, P., 2002: 'Tomography of the Solar Corona. II. Robust, Regularized, Positive Estimation of the Three-dimensional Electron Density Distribution from LASCO-C2 Polarized White-Light Images', *ApJ*, **570**, 408-422.

Frazin, R. A., Kamalabadi, F., & Weber, M. A., 2005: 'On the combination of differential emission measure analysis and rotational tomography for the analysis of solar EUV images', *ApJ*, **628**, 1070-1080.

Frazin, R. A. & Kamalabadi, F., 2005: 'On the use of total brightness measurements for tomography of the solar corona', *ApJ*, **628**, 1061-1069.

Gary, A., 1997: 'Rendering three-dimensional solar coronal structures', *Solar Phys.*, **174**, 241-263.

Gary, A., Davis, J. M., & Moore,R., 1998: 'On analysis of dual spacecraft stereoscopic observations to determine the three-dimensional morphology and plasma properties of solar coronal flux tubes', *Solar Phys.*, **183**, 45-76.

Gary, A. & Alexander, D., 1999: 'Constructing the coronal magnetic field by correlating parametrized field lines with observed coronal plasma structures', *Solar Phys.*, **186**, 123-139.

Gary, A. & Moore,R.L., 2004: 'Eruption of a multiple-turn magnetic flux tube in a large flare: evidence for external and internal reconnection that fits the break-out model of solar magnetic eruptions', *ApJ*, **611**, 545-556.

Giacalone,J., Jokipii,J.R., & Kóta,J., 2002: 'Particle acceleration in solar wind compression regions', *ApJ*, **573**, 845-850.

Gibson, S. E. & Low, B. C., 1998: 'A time-dependent three-dimensional magnetohydrodynamic model of the coronal mass ejection', *ApJ*, **493**, 460-473.

Gibson, S. E. & Low, B. C., 2000: '3D and twisted: an MHD interpretation of on-disk observational characteristics of CMEs', *JGR*, **105/A8**, 18,187-18,202.

Gopalswamy, N. & Kundu, M. R., 1993: 'Thermal and nonthermal emissions during a coronal mass ejection', *Solar Phys.*, **143**, 327-343.

Gopalswamy, N., Yashiro, S., Kaiser, M. L., Howard, R. A., & Bougeret, J.-L., H., 2001: 'Radio Signatures of Coronal Mass Ejection Interaction: Coronal Mass Ejection Cannibalism?', *ApJ*, **548**, L91-L94.

Grigoryev, V. M., 1993: 'A space-borne solar stereoscope experiment in solar physics', *Solar Phys.*, **148**, 389-391.

Groth, C. P. T., DeZeeuw, D. L., Gombosi, T. I., & Powell, K. G., 2000: 'Global three-dimensional MHD simulation of a space weather event: CME formation, interplanetary propagation, and interaction with the magnetosphere', *JGR*, **105**, 25,053.

Gudiksen, B. V. & Nordlund, A., 2002: 'Bulk heating and slender magnetic loops in the solar corona', *ApJ*, **572**, L113.

Gudiksen, B. V., & Nordlund, A., 2005a: 'An Ab Initio Approach to the Solar Coronal Heating Problem', *ApJ*, **618**, 1020-1030.

Gudiksen, B. V. & Nordlund, A., 2005b, 'An Ab Initio Approach to Solar Coronal Loops', *ApJ*, **618**, 1031-1038.

Gurnett, D. A., Baumback, M. M., & Rosenbauer, H., 1978: 'Stereoscopic direction finding analysis of a type III solar radio burst - Evidence for emission at $2f_p$', *JGR*, **83**, 616-622.

Hall, J. R., Sheth, P., DeJong, E., Lorre, J., & Liewer, P., 2004: '3D Sun loop tracer: a tool for stereoscopy of coronal loops for NASA's STEREO mission', American Geophysical Union, Fall Meeting 2004, abstract #SH21B-0422.

Howard, R. A., Moses, J. D., Socker, D. G., & The SECCHI Consortium, 2002: 'Sun Earch Connection Coronal and Heliospheric Investigation (SECCHI)', *Adv.Space Res.*, **29**, 2017-2026.

Hoeksema, J. T., 1984: 'Structure and evolution of the large scale solar and heliospheric magnetic fields', PhD Thesis, Stanford University, CA

Hudson, H. S., Lemen, J. R., St.Cyr, O. C., Sterling, A. C., & Webb, D. F., 1998: 'X-ray coronal changes during halo CMEs', *GRL*, **25**, 2481-2485.

Hurlburt, N. E., Martens, P. C. H., Slater, G. L., & Jaffey, S. M., 1994, 'Volume reconstruction of magnetic fields using solar imagery', in *Solar Active Region Evolution: Comparing Models with Observations"*, 14th Internat. Summer NSO Workshop, (eds. K. S. Balasubramaniam, and G. W.

Simon), Astronomical Society of the Pacific (ASP), San Francisco, ASP Conference Series, **68**, 30-36.

Hurlburt, N. E., Alexander, D., & Rucklidge, A. M., 2002: 'Complete Models of Axisymmetric Sunspots: Magnetoconvection with Coronal Heating', *ApJ*, **577**, 993-1005.

Ipson, S. S., Zharkova, V. V., Zharkov, S., Benkhalil, A. K., Abourdarham, J., & Fuller,N., 2005: 'Automated technique for comparison of magnetic field inversion lines with filament skeletons from the Solar Feature Catalogue', *Solar Phys.*, **228**, 399-421.

Jackson, B. V. & Froehling, H. R., 1995: 'Three-dimensional reconstruction of a coronal mass ejection', *A&A*, **299**, 885-892.

Jackson, B. V. & Hick, P. P., 2002: 'Corotational Tomography of Heliospheric Features Using Global Thomson Scattering Data', *Solar Phys.*, **211**, 345-356.

Jackson, B. V. & Hick, P. P., 2004: 'Three-dimensional tomography of interplanetary disturbances', in *"Solar and Space Weather Radiophysics"*, Astrophysics and Space Science Library Vol. 314, (eds. D. E. Gary & C. O. Keller), Kluwer Academic Publishers, Dordrecht, The Netherlands, p.355-386.

Kahler, S. W., 1997: 'Using charged particles to trace interplanetary magnetic field topology", in *"Coronal Mass Ejections"*, Proc. Chapman Conference, (eds. N.Crooker, J.Joselyn, and J.Feynman), Geophysical Monograph Series Vol. 99, American Geophysical Union (AGU), Washington DC, p.197-204.

Kano, R., & Tsuneta, S., 1995: 'Scaling law of solar coronal loops obtained with YOHKOH', *ApJ*, **454**, 934-944.

Kliem, B., Titov, V. S., & Török, T., 2004: 'Formation of current sheets and sigmoidal structure by the kink instability of a magnetic loop', *A&A*, **413**, L23-L26.

Klimchuk, J. A., 2001: 'Theory of coronal mass ejections', in *"Space Weather"*, American Geophysical Union, Geophysical Monograph Series Vol. 125, Proc. Chapman Conference on Space Weather, Clearwater, Florida, 2000 Mar 20-24, (eds. Song, P., Singer, H. J., & Siscoe, G. L), AGU, Washington DC, p.143-157.

Knock, S. A., Cairns, I. H., Robinson, P. A., & Kuncic, Z., 2001: 'Theory of type II radio emission from the foreshock of an interplanetary shock', *JGR*, **106/A11**, 25,041-25,052.

Knock, S. A., Cairns, I. H., & Robinson, P. A., 2003a: 'Type II radio emission predictions: Multiple shock ripples and dynamic spectra', *JGR*, **108/A10**, pp. SSH 2-1, CiteID 1361, DOI 10.1029/2003JA009960.

Knock, S. A., Cairns, I. H., Robinson, P. A., & Kuncic,Z., 2003b: 'Theoretically predicted properties of type II radio emission from an interplanetary foreshock', *JGR*, **108/A3**, pp. SSH 6-1, CiteID 1126, DOI 10.1029/2002JA009508.

Knock, S. A. & Cairns, I. H., 2005, 'Type II radio emission predictions: sources of coronal and interplanetary spectral structure', *JGR*, **110/A1**, CiteID A01101, DOI 10.1029/2004JA010452.

Koutchmy, S. & Molodensky, M. M., 1992: 'Three-dimensional image of the solar corona from white-light observations of the 1991 eclipse', *Nature*, **360**, 717-719.

Lamy, H., Pierrard, V., Maksimovic, M., & Lemaire, J. F. 2003: 'A kinetic exospheric model of the solar wind with a nonmonotonic potential energy for the protons', *JGR*, **108**, 1047, pp. SSH 13-1, CiteID 1047, DOI 10.1029/2002JA009487.

Lamy, P. L., Quemerais, E., Llebaria, A., Bout, M. Howard, R., Schwenn, R., & Simnett, G., 1997, 'Electronic densities in coronal holes from LASCO-C2 images', *ESA-SP*, **404**, p.491-494.

Landi, E., Landini, M., Dere, K. P., Young, P. R., & Mason, H. E., 1999: 'CHIANTI - An atomic database for emission lines. III. Continuum radiation and extension of the ion database', *A&AS*, **135**, 339-346.

Lee, J. K., Newman, T. S., & Gary, G. A. 2005: 'Oriented connectivity-based method for segmenting solar loops', Proc. 17th Internat Conf., Pattern Recognition (Journal, Elsevier), **4**, 315-328.

Lee, M. A., 2005: 'Coupled Hydromagnetic Wave Excitation and Ion Acceleration at an Evolving Coronal/Interplanetary Shock', *ApJS*, **158**, 38-67.

Liewer, P. C. , Davis, J. M., DeJong, E. M., Gary, G. A., Klimchuk, J. A., & Reinert, R. P., 1998, 'Report on new mission concept study: Stereo X-Ray Corona Imager mission', *SPIE*, **3442**, 53-64.

Liewer, P. C., DeJong, E. M., Hall, J. R., & Lorre, J., 2000: 'Stereographic analysis of coronal features for the STEREO mission', *EOS*, bf 81/48 (November 28, 2000 issue), p.F971.

Liewer, P. C., Hall, J. R., DeJong, M., Socker, D. G., Howard, R. A., Crane, P. C., Reiser, P., Rich, N., & Vourlidas, A., 2001: 'Determination of three-dimensional structure of coronal streamers and relationship to the solar magnetic field', *JGR*, **106/A8**, 15,903-15,916.

Linker, J. A., VanHoven, G., & Schnack, D. D., 1990: 'A three-dimensional simulation of a coronal streamer', *GRL*, **17/12**, 2282-2284.

Linker, J. A. & and Mikić, Z., 1995: 'Disruption of a helmet streamer by photospheric shear', *ApJ*, **438**, L45-L48.

Linker, J. A., Mikić, Z., Biesecker, D. A., Forsyth, R. J., Gibson, S. E., Biesecker, D., & Fisher, R. 1999: 'Magnetohydrodynamic modeling of the solar corona during whole sun month', *JGR*, **104/A5**, 9809-9830.

Linker, J. A., Lionello, R., Mikić, Z., & Amari, T., 2001: 'Magnetohydrodynamic modeling of prominence formation within a helmet streamer', *JGR*, **106/A11**, 25,165-25,176.

Lionello, R., Velli, M., Einaudi, G., & Mikić, Z., 1998: 'Nonlinear Magnetohydrodynamic Evolution of Line-tied Coronal Loops', *ApJ*, **494**, 840-850.

Llebaria, A., Lamy, P. L., & Koutchmy, S., 1999: 'The global activity of the solar corona', *ESA-SP*, **446**, 441-446.

Loughhead, R. E., Wang, J. L., & Blows, G., 1983: 'High-resolution photography of the solar chromosphere. XVII. Geometry of Ha flare loops observed on the disk', *ApJ*, **274**, 883-899.

Low,B.C., 1996: 'Solar activity and the corona', *Solar Phys.*, **167**, 217-265.

Lugaz, N., Manchester, W. B. IV., and Gombosi, T. I., 2005: 'The evolution of coronal mass ejection density structures', *ApJ*, **627**, 1019-1030.

Luhmann, J. G., Solomon, S. C., Linker, J. A., Lyon, J. G., Mikić, Z., Odstrčil, D., Wang, W., & Wiltberger, M., 2004: 'Coupled model simulation of a Sun-to-Earth space weather event', J.Atmos.Solar-Terr.Phys., (in press).

McLean, D. J. & Labrum, N. R. (eds.), 1985: *Solar Radiophysics*, Cambridge University Press, Cambridge.

Manchester, W. IV., 2003: 'Buoyant disruption of magnetic arcades with self-induced shearing', *JGR*, **108/A4**, 1162, SSH 10-1, DOI 10.1029/2002JA009252.

Manchester, W. IV., Gombosi, T. I., Roussev, I., DeZeeuw, D. L., Sokolov, I. V., Powell, K. G., Toth, G., & Opher, M., 2004a: 'Three-Dimensional MHD Simulation of a Flux Rope Driven CME', *JGR*, **109/A1**, A01102.

Manchester, W. IV., Gombosi, T., DeZeeuw, D., & Fan, Y., 2004b: 'Eruption of a buoyantly emerging magnetic flux rope', *ApJ*, **610**, 588-596.

Mikić, Z. & Linker, J. A., 1994: 'Disruption of coronal magnetic field arcades', *ApJ*, **430**, 898-912.

Mikić, Z., Linker, J. A., Schnack, D. D., Lionello, R., & Tarditi, A., 1999: 'Magnetohydrodynamic modeling of the global solar corona', *Phys. Plasmas*, **6/No. 5**, 2217-2224.

Milne, E. A., 1921: 'Radiative equilibrium in the outer layers of a star', *MNRAS*, **81**, 361-375.

Minnaert, M., 1930: 'On the continuous spectrum of the corona and its polarisation', *Zeitschrift fur Astrophysik*, **1**, 209.

Mok, Y., Mikić, Z., Lionello, R., & Linker, J. A., 2005: 'Calculating the Thermal Structure of Solar Active Regions in Three Dimensions', *ApJ*, **621**, 1098-1108.

Moran, T. G. & Davila, J. M., 2004: 'Three-Dimensional Polarimetric Imaging of Coronal Mass Ejections', *Science*, **305**, 66-71.

Mueller, J. T., Maldonado. H., & Driesman, A. S., 2003: 'STEREO: The challenges', *Acta Astronautica*, **53**, 729-738.

Neckel, N. & Labs, D., 1994: 'Solar limb darkening 1986-1990', *Solar Phys.*, **153**, 91-114.

Nelson, G. J. & Melrose, D. B., 1985: 'Type II bursts', in *"Solar Radiophysics"*, (eds. McLean, D. J. & Labrum, N. R.), Cambridge University Press, Cambridge, p. 333-359.

Ng, C. K., Reames, D. V., & Tylka, A. J., 1999: 'Effect of proton-amplified waves on the evolution of solar energetic particle composition in gradual events', *GRL*, **26**, 2145-2148.

Ng, C. K., Reames, D. V., & Tylka, A. J., 2003: 'Modeling Shock-accelerated Solar Energetic Particles Coupled to Interplanetary Alfvén Waves', *ApJ*, **591**, 461-485.

Neugebauer, M., 2001: 'The solar-wind and heliospheric magnetic field in three dimensions', in *"The Heliosphere Near Solar Minimum - The Ulysses perspective"*, Springer-Praxis Books in Astrophysics and Astronomy, (eds. Balogh,A., Marsden,R.G. and Smith,E.J.), p.43-106.

Odstrčil, D., 1994: 'Interactions of solar wind streams and related small structures', *JGR*, **99/A9**, 17,653-17,671.

Odstrčil, D., Dryer, M., & Smith,Z., 1996: 'Propagation of an interplanetary shock along the heliospheric plasma sheet', *JGR*, **101**, 19,973-19,984.

Odstrčil, D. & Pizzo,V.J., 1999a: 'Distortion of the interplanetary magnetic field by three-dimensional propagation of coronal mass ejections in a structured solar wind', *JGR*, **104/A12**, 28,225-28,239.

Odstrčil, D. & Pizzo,V.J., 1999b: 'Three-dimensional propagation of CMEs in a structured solar wind flow: 1. CME launched within the streamer belt', *JGR*, **104/A1**, 483-492.

Odstrčil, D. & Pizzo,V.J., 1999c: 'Three-dimensional propagation of CMEs in a structured solar wind flow: 2. CME launched adjacent to the streamer belt', *JGR*, **104/A1**, 493-504.

Odstrčil, D. & Karlický, M., 2000: 'Propagation of shock waves in the solar corona with 2-D loop structures', *A&A*, **359**, 766-776.

Odstrčil, D., Linker, J. A., Lionello, R., Mikić, Z., Riley, P., Pizzo, V. J., & Luhmann,J.G., 2002: 'Merging of coronal and heliospheric numerical two-dimensional MHD models', JGR 107/A12, SSH 14-1, CiteID 1493, DOI 10.1029/2002JA009334.

Odstrčil, D., 2003: 'Modeling 3D solar wind structure', *Adv. Space Res.*, **32/4**, 497-506.

Odstrčil, D., Riley, P., & Zhao, X .P., 2004a: 'Numerical simulation of the 12 May 1997 interplanetary CME event', *JGR*, **109/A2**, CideID A02116, DOI 10.1029/2003JA010135.

Odstrčil, D., Pizzo, V. J., Linker, J. A., Riley, P., Lionello, R., & Mikić, Z., 2004b: 'Initial coupling of coronal and heliospheric numerical magnetohydrodynamic codes', *J.Atmos.Solar-Terr.Phys.*, (in press).

Odstrčil, D., Pizzo, V. J., & Arge, C. N., 2005: 'Propagation of the 12 May 1997 interplanetary coronal mass ejection in evolving solar wind structures', *JGR* (Space Physics), **110**, 2106, CiteID A02106, DOI 10.1029/2004JA010745.

Pick, M., Maia, D., Kerdraon, A., Howard, R. A., Brueckner, G. E., Michels, D. J. Paswaters, S., Schwenn, R., Lamy, P., Llebaria, A., Simnett, G., Lanzerotti, L. J., & Aurass, H., 1998: 'Joint Nancay radioheliograph and LASCO observations of coronal mass ejections. II. The 9 July 1996 event', *Solar. Phys.*, **181**, 455-468.

Pizzo, V. J. (ed.), 1994: 'The findings of the SPINS science workshop', SEL Workshop Report January 1994, *"SPINS : Special Perscpectives Investigations"*, NOAA/SEL, Boulder, Colorado, on November 3-5, 1993.

Pizzo, V. J. & Biesecker, D. A., 2004, 'Geometric localization of STEREO CMEs', *GRL*, **31**, 21,802.

Podladchikova, O. V., & Berghmans, D., 2005: 'Automated detection of EIT waves and dimmings', *Solar Phys.*, **228**, 265-284.

Portier-Fozzani, F. & Inhester,B., 2001: '3D coronal structures and their evolutions measured by stereoscopy, consequences for space weather and the STEREO mission', *Space Sci. Rev*, **97**, 1/4, 51-54.

Portier-Fozzani, F. & Inhester,B., 2002: 'Inputs in the 3D observations of the magnetic corona from SOHO to STEREO of the epipolar geometry', in *"Magnetic Coupling of the Solar Atmosphere"*, Proc. Euroconference and IAU Colloquium 188, ESA, ESTEC Noordwijk, The Netherlands, *ESA-SP*, **505**, 545-548.

Powell, K. G., Roe, P. L., Linde, T. J., Gombosi, T. I., & deZeeuw, D. L., 1999: 'A Solution-Adaptive Upwind Scheme for Ideal Magnetohydrodynamics', *J.Comp.Phys.*, **154**, 284-309.

Puetter, R. C., 1995: 'Pixon-based multiresolution image reconstruction and the quantification of picture information content', *Int. J. Image Sys. & Tech.*, **6**, 314-331.

Puetter, R. C., 1996: 'Information, language, and pixon-based Bayesian image reconstruction in digital image recovery and synthesis III', *SPIE*, **2827**, 12-31.

Puetter, R. C., 1997: 'Modern methods of image reconstruction', in *"Instrumentation for large telescopes"*, (eds. J.M.Rodriguez Espinosa, A.Herrero, and F.Sanchez), Cambridge University Press: New York, p.75-122.

Puetter, R. C. & Yahil, A., 1999: 'The pixon method of image reconstruction', in *"Astronomical Data Analysis Software and Systems VIII"*, (eds. D.M.Mehringer, R.L.Plante, and D.A.Roberts), *ASP* Conference Series **172**, 307-316.

Quémerais, E. & Lamy, P., 2002: 'Two-dimensional electron density in the solar corona from inversion of white light images - Application to SOHO/LASCO-C2 observations', *A&A*, **393**, 295-304.

Reames, D.V., 1997: 'Energetic particles and the structure of coronal mass ejections', in *"Coronal Mass Ejections"*, Proc. Chapman Conference, (eds. N.Crooker, J.Joselyn, and J.Feynman), Geophysical Monograph Series Vol. 99, American Geophysical Union (AGU), Washington DC, p.217-226.

Reiner, M. J. & Stone, R. G., 1986: 'A new method for reconstructing type III trajectories', *Solar Phys.*, **100**, 397-401.

Reiner, M. J. & Stone, R. G., 1988: 'Model interpretation of type III radio burst characteristics: I.spatial aspects', *A&A*, **206**, 316-335.

Reiner, M. J. & Stone, R. G., 1989: 'Model interpretation of type III radio burst characteristics: II.temporal aspects', *A&A*, **217**, 251-269.

Reiner, M. J., Kaiser, M. L., Fainberg,J., Bougeret, J.-L., Stone, R. G., 1998a: 'On the origin of radio emissions associated with the January 6-11, 1997, CME', *GRL*, **25/14**, 2493-2496.

Reiner, M. J., Fainberg, J., Kaiser, M. L., Stone, R. G., 1998b: 'Type III radio source located by Ulysses/Wind triangulation', *JGR*, **103**, 1923.

Reiner, M. J. & Kaiser, M. L., 1999: 'High-frequency type II radio emissions associated with shocks driven by coronal mass ejections', *JGR*, **104/A8**, 16,979-16,992.

Riley, P., Linker, J. A., & Mikić, Z. 2001a: 'An empirically-driven global MHD model of the corona and inner heliosphere', *JGR*, **106/A8**, 15,889-15,902.

Riley, P., Linker, J. A., & Mikić, Z., & Lionello,R., 2001b: 'MHD Modeling of the Solar Corona and Inner Heliosphere: Comparison with Observations', in *Space Weather*, Geophysical Monograph Series, (eds., Song, P., Singer, H. J., & Siscoe, G. L.), Vol. 125, p.159-167.

Riley, P., Linker, J. A., & Mikić, Z., 2002a: 'Modeling the heliospheric current sheet: Solar cycle variations', *JGR*, **107/A7**, DOI 10.1029/2001JA000299.

Riley, P., Linker, J. A., & Mikić, Z., Odstrcčil, D., Pizzo, V. J., & Webb, D. F., 2002b: 'Evidence of Posteruption Reconnection Associated with Coronal Mass Ejections in the Solar Wind', *ApJ*, **578**, 972-978.

Riley, P., Mikić, Z., & Linker, J. A., 2003a: 'Dynamical evolution of the inner heliosphere approaching solar activity maximum: Interpreting Ulysses observations using a global MHD model', *Ann. Geophys. J.*, **21**, 1347.

Riley, P., Linker, J. A., & Mikić, Z., Odstrčil, D., Zurbuchen, T. H., Lario, D., & Lepping, R. P., 2003b: 'Using an MHD simulation to interpret the global context of a coronal mass ejection observed by two spacecraft', *JGR*, **108/A7**, SSH 2-1, CiteID 1272, DOI 10.1029/2002JA009760.

Riley, P., Linker, J. A., Lionello, R., Mikić, Z., Odstrčil, D., Hidalgo, M. A., Hu, Q., Lepping, R. P., Lynch, B. J., & Rees, A., 2004: 'Fitting flux ropes to a global MHD solution: a comparison of techniques', *J.Atmos.Solar-Terr.Phys.*, **66**, 1321-1331.

Riley, P. & Crooker, N. U., 2004: 'Kinematic Treatment of Coronal Mass Ejection Evolution in the Solar Wind', *ApJ*, **600**, 1035-1042.

Robinson, P. A. & Cairns, I. H., 1998a: 'Fundamental and harmonic emission in type III solar radio bursts: I. Emission at a single location or frequency', *Solar Phys.*, **181**, 363-394.

Robinson, P. A. & Cairns, I. H., 1998b: 'Fundamental and harmonic emission in type III solar radio bursts: II. Dominant modes and dynamic spectra', *Solar Phys.*, **181**, 395-428.

Robinson, P. A. & Cairns, I. H., 1998c: 'Fundamental and harmonic emission in type III solar radio bursts: III. Heliocentric variation of interplanetary beam and source parameters', *Solar Phys.*, **181**, 429-437.

Robbrecht, E. & Berghmans, D., 2004: 'Automated recognition of coronal mass ejections (CMEs) in near-real-time data', *A&A*, **425**, 1097-1106.

Rosner, R., Tucker, W. H., & Vaiana, G. S., 1978: 'Dynamics of quiescent solar corona', *ApJ*, **220**, 643-665.

Roussev, I. I., Gombosi, T. I., Sokolov, I. V., Velli, M., Manchester, W., DeZeeuw, D.'L., Liewer, P., Toth, G., & Luhmann, J., 2003a: 'A Three-dimensional Model of the Solar Wind Incorporating Solar Magnetogram Observations', *ApJ*, **595**, L57-L61.

Roussev, I. I., Forbes, T. G., Gombosi, T. I., Sokolov, I. V., DeZeeuw, D. L., & Birn, J., 2003b: 'A Three-dimensional Flux Rope Model for Coronal Mass Ejections Based on a Loss of Equilibrium', *ApJ*, **588**, L45-L48.

Roussev, I. I., Sokolov, I. V., Forbes, T. G., Gombosi, T. I., Lee, M. A., & Sakai,J.I., 2004: 'A numerical model of a coronal mass ejection: shock development with implications for the acceleration of GeV protons', *ApJ*, **605**, L73-L76.

Roussev, I. I., & Sokolov, I. V., 2005: 'Models of Solar Eruptions: Recent Advances From Theory and Simulations', in "Solar Eruptions and Energetic Particles", Chapman Conf., Turku, Finland, 2-6 Aug 2004, (eds. N. Gopalswamy, R. Mewaldt, and J. Torsti), Geophysical Monograph Series, AGU, Washington DC, (in press).

Rust, D. M. & Kumar, A., 1996: 'Evidence for helically kinked magnetic flux ropes in solar eruptions', *ApJ*, **464**, L199-L202.

Rust, D. M. et al. (eds.), 1997: 'The sun and heliosphere in three dimensions', Report of the NASA Science Definition Team for the STEREO Mission, edited and published at John Hopkins Univ. Applied Physics Lab., Laurel, Maryland, 1997 Dec 1.

Rust, D. M. & LaBonte, B., 2005: 'Observational evidence of the kink instability in solar filament eruptions and sigmoids', *ApJ*, **622**, L69-L72.

Schatten, K. H., Wilcox, J. M., & Ness, N. F., 1969: 'A model of interplanetary and coronal magnetic fields', *Solar Phys.*, **6**, 442-455.

Schmidt, W. K. H. & Bothmer, V., 1996: 'Stereoscopic viewing of solar coronal and interplanetary activity', *Adv. Space Res.*, **17**, 369-376.

Schrijver, C. J. & DeRosa, M. L., 2003: 'Photospheric and heliospheric magnetic fields', *Solar Phys.*, **212**, 165-200.

Schrijver, C. J., Sandman, A. W., Aschwanden, M. J., & DeRosa, M. L., 2004: 'The coronal heating mechanism as identified by full-Sun visuzliations', *ApJ*, **615**, 512-525.

Schwenn, R. & Marsch, E. (eds.), 1991a: 'Physics of the inner heliosphere. I. Large-scale phenomena', Springer-Verlag Berlin, 282p.

Schwenn, R. & Marsch, E. (eds.), 1991b: 'Physics of the inner heliosphere. II. Particles, waves and turbulence', Springer-Verlag Berlin, 352p.

Serio, S., Peres, G., Vaiana, G. S., Golub, L., & Rosner, R., 1981: 'Closed coronal structures. II generalized hydrostatic model', *ApJ*, **243**, 288-300.

Socker, D. G. et al., 1996: 'STEREO: A solar terrestrial event observer mission concept', *SPIE*, **2804**, 50-61.

Socker, D. G., 1998: 'Stereographic image potential of a STEREO mission', *SPIE*, **3442**, 44-52.

Socker, D. G. et al., 2000: 'NASA Solar Terrestrial Relations Observatory (STEREO) mission', *SPIE*, **4139**, 284-293.

Sokolov, I. V., Timofeev, E. V., Sakai, J. I., and Takayama, K., 2002: 'Artificial Wind-A New Framework to Construct Simple and Efficient Upwind Shock-Capturing Schemes', *J.Comp.Phys.*, **181**, 354.

Sokolov, I. V, Roussev, I. I., Gombosi, T. I., Lee, M. A., Kóta, J., Forbes, T. G., Manchester, W. B., & Sakai, J. I., 2004: 'A New Field Line Advection Model for Solar Particle Acceleration', *ApJ*, **616**, L171-L174.

Steinolfson, R. S. & Hundhausen, A. J., 1988: 'Density and white light brightness in looplike coronal mass ejections - Temporal evolution', *JGR*, **93**, 14,269-14,276.

Stewart, R. T., 1984: 'Association of type II soalr radio bursts with coronal structures above H-alpha filament channels', *Solar Phys.*, **94**, 379-385.

Thompson, B. J., Gurman, J. B., Neupert, W. M., Newmark, J. S., Delaboudiniere, J. P., St.Cyr, O. C., Stezelberger, S., Dere, K. P., Howard, R. A., & Michels, D. J., 1999: 'Soho/EIT observations of the 1997 April 7 coronal transient: possible evidence of coronal Moreton waves', *ApJ*, **517**, L151-154.

Titov, V. S. & Démoulin, P., 1999: 'Basic topology of twisted magnetic configurations in solar flares', *A&A*, **351**, 707-720.

Török, T. & KIiem, B., 2003: 'The evolution of twisting coronal magnetic flux tubes', *A&A*, **406**, 1043-1059.

Török, T., KIiem, B., & Titov, V. S., 2003: 'Ideal kink instability of a magnetic loop equilibrium', *A&A*, **413**, L27-L30.

Török, T. & KIiem, B., 2004: 'The kink instability in solar eruptions', in *"Coronal Heating"*, SOHO-15 Workshop, ESA, ESTEC Noordwijk, The Netherlands, *ESA-SP*, **575**, 56-61.

Toth,G., 1996; 'A General Code for Modeling MHD Flows on Parallel Computers: Versatile Advection Code', *Astrophys. Lett. Comm.*, **34**, 245.

Toth, G. & Odstrčil, D., 1996: 'Comparison of some flux corrected transport and total variation diminishing numerical schemes for hydrodynamic and magnetohydrodynamic problems', *J. Comput. Phys.*, **182**, 82-100.

Tripathi, D., Bothmer, V., & Cremades,H., 2004: 'The basic characteristic of EUV post-eruptive arcades and their role as tracers of coronal mass ejection source regions', *A&A*, **422**, 337-350.

Tylka, A. J., Reames, D. V., and Ng, C. K., 1999: 'Observations of systematic temporal evolution in elemental composition during gradual solar energetic particle events', *GRL*, **26/14**, 2141-2144.

Tylka, A. J., Cohen, C. M. S., Dietrich, W. F., Lee, M. A., Maclennan, C. G., Mewaldt, R. A., Ng, C. K., & Reames, D. V., 2005: 'Shock Geometry, Seed Populations, and the Origin of Variable Elemental Composition at High Energies in Large Gradual Solar Particle Events', *ApJ*, **625**, 474-495.

Van de Hulst, H. C., 1950: 'The electron density of the solar corona', *Bull. Astron. Inst. Neth.*, **11**, 135.

Vedenov, A. A., Koutvitsky, V. A., Koutchmy, S., Molodensky, M. M., & Oraevsky, V. N., 2000: 'On stereoimages of some structures in the solar atmosphere', *Astronomy Reports*, **44/2**, 112-121.

Vourlidas, A., Subramanian, P., Dere, K. P., & Howard, R. A., 2000: 'Large-angle spectrometric coronagraph measurements of the energetics of coronal mass ejections', *ApJ*, **534**, 456-467.

Wang, Y. M. & Sheeley, N. R. Jr., 1992: 'On potential-field models of the solar corona', *ApJ*, **392**, 310-319.

Wang, Y. M., 2000: 'EIT waves and fast-mode propagation in the solar corona', *ApJ*, **543**, L89-L93.

Warmuth, A., & Mann, G., 2005: 'A model of the Alfven speed in the solar corona', *A&A*, **435**, 1123-1135.

Webb, D. F., Burkepile, J., Forbes, T. G., & Riley,P., 2003: 'Observational evidence of new current sheets trailing CMEs', *JGR*, **108/A12**, SSH 6-1, CiteID 1440, DOI 10.1029/2003JA009923.

Wiegelmann, T. & Neukirch, T., 2002: 'Including stereoscopic information in the reconstruction of coronal magnetic fields', *Solar Phys.*, **208**, 233-251.
Wiegelmann, T. & Inhester, B., 2003: 'Magnetic modeling and tomography: First steps towards a consistent reconstruction of the solar corona', *Solar Phys.*, **214**, 287-312.
Wiegelmann, T., Lagg, A., Solanki, S. K., Inhester, B., & Woch, J., 2005: 'Comparing magnetic field extrapolations with measurements of magnetic loops', *A&A*, **433**, 701-705.
Wiegelmann, T., Inhester, B., Lagg,A., & Solanki, S., 2005: 'How to use magnetic field information for coronal loop identification', *Solar Phys.*, **228**, 67-79.
Wild, J. P., Smerd, S. F., & Weiss, A. A., 1963: 'Solar bursts', *Annual Rev. Astron. Astrophys.*, **1**, 291-366.
Winebarger, A. R., Warren, H., VanBallegooijen, A., DeLuca, E., & Golub, L., 2002: 'Steady flow detected in EUV loops', *ApJ*, **567**, L89-L92.
Wood, B. E., Karovska, M., Chen, J., Brueckner, G. E., Cook, J. W., & Howard, R. A., 1999: 'Comparison of two coronal mass ejections observed by EIT and LASCO with a model of an erupting magnetic flux rope', *ApJ*, **512**, 484-495.
Wu, S. T., Zheng, H., Wang, S., Thompson, B. J., Plunkett, S. P., Zhao, X. P., & Dryer, M., 2001: 'Three-dimensional numerical simulation of MHD waves observed by the Extreme Ultraviolet Imaging Telescope', *JGR*, **106**, 25,089-25,102.
Young, P. R., Landi, E., & Thomas, R. J., 1998: 'CHIANTI: an atomic database for emission lines. II. Comparison with the SERTS-89 active region spectrum', *A&A*, **329**, 391-314.
Zank, G. P. & Li, G., 2004: 'Particle acceleration at CME-driven shocks: why the injection problem is important', in Proc. 35th COSPAR Scientific Assembly, 18-25 July 2004, Paris, France, p.295.
Zeldovich, Ya. B. and Raizer, Yu. P., 2002: 'Physics of Shock Waves and High-Temperature Hydrodynamic Phenomena', (eds. W. D. Hayes and R. F. Probstein), Mineola, Dover.
Zhang, M. & Low, B. C., 2005: 'The hydromagnetic nature of solar coronal mass ejections', *Annual Rev. Astron. Astrophys.*, **43**, 103.
Zharkova, V. V. & Schetinin, V., 2005: 'Filament recognition in solar images with artificial neural network', *Solar Phys.*, **228**, 137-148.
Zidowitz, S., Inhester, B., & Epple, A., 1996: 'Tomographic inversion of coronagraph images', in *"Solar Wind Eight"*, Internat. Solar Wind Conference, (eds., D. Winterhalter, J. T. Gosling, S. R. Habbal, W. S. Kurth, & M. Neugebauer), AIP Press, New York, American Institute of Physics Conference Proceedings *AIP-CP*, **382**, 165-166.
Zidowitz, S., 1997: 'The coronal structure in August 1996 - A tomographic reconstruction', in *"The Corona and Solar Wind Near Minimum Activity"*, Proc. 5th SoHO Workshop, (ed. Wilson,A.), European Space Agency, ESTEC Noordwijk, The Netherlands, *ESA-SP*, **404**, 757-761.
Zidowitz, S., 1999: 'Coronal structure of the whole sun month: a tomographic reconstruction', *JGR*, **104/A5**, 9727-9734.

Address for Offprints: Markus J. Aschwanden, Solar & Astrophysics Lab., Lockheed Martin ATC, Org. ADBS, Bldg. 252, 3251 Hanover St., Palo Alto, CA 94304, USA; aschwanden@lmsal.com; URL=http://www.lmsal.com/~aschwand/